Advances in Physics: X

ISSN: (Print) 2374-6149 (Online) Journal homepage: http://www.tandfonline.com/loi/tapx20

Development and application of radar reflectometer using micro to infrared waves

A. Mase, Y. Kogi, D. Kuwahara, Y. Nagayama, N. Ito, T. Maruyama, H. Ikezi, X. Wang, M. Inutake, T. Tokuzawa, J. Kohagura, M. Yoshikawa, S. Shinohara, A. Suzuki, F. Sakai, M. Yamashika, B. J. Tobias, C. Muscatello, X. Ren, M. Chen, C. W. Domier & N. C. Luhmann Jr.

To cite this article: A. Mase, Y. Kogi, D. Kuwahara, Y. Nagayama, N. Ito, T. Maruyama, H. Ikezi, X. Wang, M. Inutake, T. Tokuzawa, J. Kohagura, M. Yoshikawa, S. Shinohara, A. Suzuki, F. Sakai, M. Yamashika, B. J. Tobias, C. Muscatello, X. Ren, M. Chen, C. W. Domier & N. C. Luhmann Jr. (2018) Development and application of radar reflectometer using micro to infrared waves, Advances in Physics: X, 3:1, 1472529, DOI: 10.1080/23746149.2018.1472529

To link to this article: https://doi.org/10.1080/23746149.2018.1472529

ADVANCES IN PHYSICS: X, 2018
VOL. 3, NO. 1, 1472529
https://doi.org/10.1080/23746149.2018.1472529

Taylor & Francis
Taylor & Francis Group

REVIEW ARTICLE

OPEN ACCESS Check for updates

Development and application of radar reflectometer using micro to infrared waves

A. Mase[a,b], Y. Kogi[b], D. Kuwahara[c], Y. Nagayama[d], N. Ito[e], T. Maruyama[f], H. Ikezi[a], X. Wang[g], M. Inutake[h], T. Tokuzawa[d], J. Kohagura[i], M. Yoshikawa[i], S. Shinohara[c], A. Suzuki, F. Sakai[j], M. Yamashika[k], B. J. Tobias[l], C. Muscatello[m], X. Ren[n], M. Chen[n], C. W. Domier[n] and N. C. Luhmann Jr.[n]

[a]Global Innovation Center, Kyushu University, Kasuga, Japan; [b]Fukuoka Institute of Technology, Fukuoka, Japan; [c]Institute of Engineering, Tokyo University of Agriculture and Technology, Tokyo, Japan; [d]National Institute for Fusion Science, Toki, Japan; [e]National Institute of Technology, Ube College, Ube, Japan; [f]Faculty of Arts and Science, Kyushu University, Kasuga, Japan; [g]State Key Laboratory of Integrated Optelectronics, College of Electronic Science and Engineering, Jilin University, Changchun, China; [h]Research Institute of Electrical Communication, Tohoku University, Sendai, Japan; [i]Plasma Research Center, University of Tsukuba, Tsukuba, Japan; [j]Sakura Tech Co., Yokohama, Japan; [k]Subaru Co., Utsunomiya, Japan; [l]Los Alamos National Laboratory, Los Alamos, NM, USA; [m]General Atomics, San Diego, CA, USA; [n]Electrical & Computer Engineering Department, University of California, Davis, CA, USA

ABSTRACT

Progress in microwave and millimeter-wave technologies has made possible advanced diagnostics for application to various fields, including radio astronomy, alien substance detection, plasma diagnostics, airborne and space-borne imaging radars called as synthetic aperture radars, and living body measurements. Transmission, reflection, scattering, and radiation processes of electromagnetic waves are utilized as diagnostic principles. The diagnostics are classified as active and passive systems. Specifically, active radar reflectometry has become of importance in various applications due to the possibility of high localization and accessibility of the measurements as well as the non-invasive nature of the systems. In this paper, recent development and application of radar reflectometers are described. The key words are profile reflectometry, fluctuation reflectometry, imaging radar (optics imaging and synthetic aperture imaging), and radio-optics fusion technology in order to improve the spatial resolution.

ARTICLE HISTORY
Received 20 November 2017
Accepted 25 April 2018

KEYWORDS
Electromagnetic waves; radar reflectometry; imaging; plasma; biomedical measurement; remote sensing

PACS
07.57.-c: Infrared to microwave instruments; 52.35.-q: Waves and instabilities in plasmas; 52.70.GW: Plasma diagnostics with microwave; 87.57.-s: Medical imaging; 93.85.Pq: Remote sensing; 93.85.-q: Instruments and techniques

CONTACT A. Mase mase@gic.kyushu-u.ac.jp

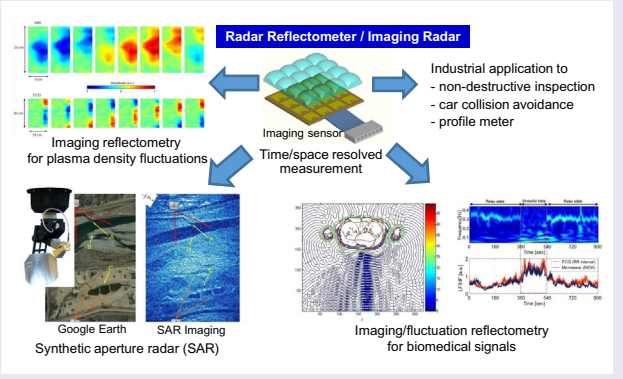

1. Introduction

Radar (radio detection and ranging) is a well-known measurement technique that employs electro-magnetic waves to determine the direction and position of unknown objects. Radar was first applied for military usage with great success. Application to remote sensing and in-vehicle systems for collision avoidance and automatic cruise control has also been extremely fruitful due to the high transmissivity of microwaves under various atmospheric conditions in comparison with infrared and visible light. Recently, radar systems have been utilized in various fields because the diagnostic systems have the features of (i) good accessibility, (ii) non-invasive nature, as well as (iii) good spatial resolution in the range direction. In the present paper, we focus on the development of radar reflectometry and its application to fusion plasma diagnostics (Section 3), biomedical signal detection (Section 4), and remote sensing (Section 5), all of which make use of the above mentioned features. Here, the progress in microwave and millimeter-wave devices and circuits, such as monolithic microwave integrated circuits (MMICs), and data processing including computer technology has contributed to the rapid advancement in radar diagnostic technology for the understanding of physics issues in the above-mentioned fields.

All of the above-mentioned features are extremely important for fusion plasma diagnostics and depend upon specific characteristics in plasmas, such as the cut-off density. Here, when an electromagnetic wave is launched into a plasma, the wave is reflected at the corresponding cut-off layer. The frequency corresponding to the cut-off in plasmas of fusion interest typically spans the microwave to millimeter wave region. Due to the high degree of localization of the measurements and modest requirements for diagnostic port window access, radar reflectometry has become a common diagnostic of high density plasmas, and it is now utilized on a number of magnetic fusion devices.

Microwave/millimeter-wave reflectometry has also become of importance in various biomedical measurements, specifically due to its non-invasive nature. Two characteristics of microwave/millimeter-wave diagnostic systems combine to act effectively. The first is the penetration characteristics through dielectric materials. The second is the use of sensitive phase fluctuation measurements. These features are appropriate for biomedical imaging while maintaining appropriate spatial resolution. The use of fluctuation reflectometry can be applied to the measurement of periodic movements such as vital signals since the phase fluctuation can be detected using the Doppler effect.

As is emphasized above, microwave/millimeter-wave radar has good spatial resolution in the range direction although the cross-range (azimuth) resolution is rather poor compared to visible light and X-ray due to its wavelength. One of the methods developed for further improvement of the resolution is synthetic aperture radar (SAR) technology. In this paper, two methods are introduced, that is, a motion-compensated spotlight-mode SAR and a microwave-modulated laser radar. The limitation of the spatial resolution will be overcome by use of those technologies.

The subjects to be introduced in this review are only a few examples of the many applications of radar reflectometry, in which the authors have been engaged as joint programs among universities and national projects. Industry–university collaboration programs have also been carried out in relation to application studies of reflectometry. For example, from the viewpoint of consumer use, one of the attractive examples may be non-destructive inspection for alien substances and of abnormal existence in an object. In the present stage, the minimum detectable size is typically estimated as $\lambda/2$ (λ is the incident wavelength in the object). However, the detectable size can be reduced to less than the diffraction limit level by a combination of new technology such as metamaterials and metalenses. The microwave/millimeter-wave to infrared wave reflectometry can be utilized complementarily with existing diagnostic methods using X-ray, visible light, and supersonic waves while keeping good transmission properties under various environment.

2. Radar reflectometry

The radar (radio detecting and ranging) technique has been applied as a means to detect the distance and the direction to an object. Three types of radar systems are mainly utilized, those being: frequency-modulated continuous-wave (FM-CW) radar, pulse radar, and fixed-frequency Doppler radar.

2.1. FM-CW radar

The basic conception of FM-CW radar is shown in Figure 1(a) [1]. The CW output is modulated by a chirped wave with repetition period of T_m as

$$S_1(t) = a_1 \cos\phi(t) \tag{1}$$

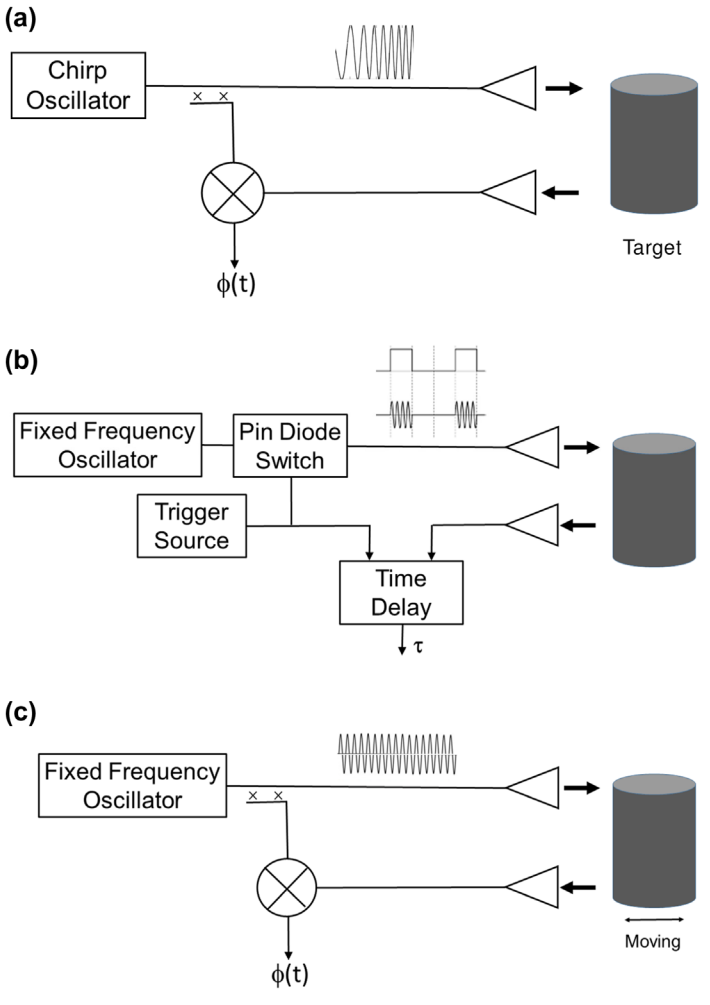

Figure 1. Schematic of the radar system: (a) FM-CW radar, (b) pulse radar, (c) Doppler radar.

where $\phi(t) = 2\pi f_c t + \pi\left(B/T_m\right)t^2$, is the phase component, f_c is the frequency offset, and B is the frequency sweep width. The instantaneous frequency of the transmitted wave is given by

$$F(t) = \frac{1}{2\pi} \cdot \frac{d}{dt}\phi(t) = f_c + \frac{B}{T_m}t. \tag{2}$$

During the time interval (0, T_m), the radar frequency linearly varies between f_c and $f_c + B$. When the output wave is reflected by a target located at a distance R, the reflected wave is given by

$$S_2(t) = a_2 \cos\phi(t - \tau), \tag{3}$$

where $\tau = 2R/c$ is the round trip time of the reflected wave, and c is the speed of light.

The mixer output, the intermediate frequency (IF) signal between the reflected wave and the reference wave split from the source output using a power divider or a directional coupler, is given by

$$S_3(t) = a_3\cos[\phi(t) - \phi(t-\tau)] = a_3\cos\left(2\pi f_{IF}t + 2\pi f_c\tau - \frac{\pi B}{T_m}\tau^2\right), \quad (4)$$

where $f_{IF} = B\tau/T_m = 2Bf_mR/c$ is the beat frequency, $f_m = T_m^{-1}$ is the radar repetition frequency,

In FM-CW radar, the target position is evaluated by performing Fourier analysis of the mixer output signal. Using a Fourier transform with a rectangular window with time interval of T_m, the mixer output signal is shown as

$$S_r = P_r\left[\frac{\sin\{\pi(f - f_{IF})T_m\}}{\pi(f - f_{IF})T_m}\right]^2, \quad (5)$$

where f is the analysis frequency and $P_r = a_3{}^2$ is the power of the reflected wave. From the standard radar equation, the reflected wave P_r can be written as (Friis' equation)

$$P_r = P_t\frac{\sigma G_tG_r\lambda^2}{(4\pi)^3R^4}, \quad (6)$$

where P_t is the power of transmitted wave [W], σ is the radar cross-section [m^2], λ is the wavelength of the radar [m], and G_t and G_r are the gains of transmitter and receiver antennas, respectively.

The target position (range distance) is evaluated by performing Fourier analysis of the beat frequency. Since the detectable frequency is limited by the duration of the repetition time. The resolution in the range direction of FM-CW radar is determined by the frequency change given by the time limit of $f_{IF} = f_m = T_m^{-1}$. Therefore, the resolution is given by

$$2B\Delta R/c = 1, \quad \Delta R = c/2B. \quad (7)$$

2.2. Pulse radar

In contrast to the FM-CW radar, the output signal transmits an intermittent signal with alternate on- and off-periods as shown in Figure 1(b). The waveform of an output wave is described by an amplitude modulated fixed frequency wave given by

$$S_1(t) = b_1(t)\cos 2\pi f_c t, \quad (8)$$

where $b_1(t)$ has the shape of the repetition pulse. The reflected wave from a target located at the distance R experiences a round trip delay time of$\tau = 2R/c$. In order to resolve the distance, this delay time has to be larger than the duration time of the pulse $\Delta\tau$. Therefore, the resolution in the range direction is given by

$$2\Delta R/c = \Delta\tau, \ \Delta R = c\,\Delta\tau/2. \tag{9}$$

The distance to the target is evaluated from the time difference between the incident wave and the reflected wave. It is shown that the shorter the transmission pulse width the better the resolution is. In order to obtain comparable spatial resolution with an FM-CW radar, a periodic pulse with each duration time of $\Delta\tau$~$1/B$ is needed.

2.3. Fixed-frequency (Doppler) radar

The Doppler radar shown in Figure 1(c) utilizes a Doppler effect produced by the movement of a target. Compared to the transmitted wave, the frequency of the reflected wave becomes higher during the approach of the target and lower during the recession. The beat frequency between the transmitted wave and the reflected wave gives the information of target movement. A fixed-frequency source can be utilized for this purpose.

The distance to a target is given by $R \pm vt$ when the target is moving with a velocity of v. The reflected wave from a target is given by

$$\begin{aligned} &S_2(t) = c_2\cos\phi(t), \\ &\phi(t) = 2\pi f_c t - 2k(R \pm vt) = 2\pi\left(f_c \mp \frac{2v}{\lambda}\right)t - 2kR \end{aligned} \tag{10}$$

and the frequency shift is given by

$$f_d = 2v/\lambda. \tag{11}$$

The reflected wave is down converted to the intermediate frequency (IF) wave at a mixer. It is difficult to identify the increase or decrease of phase giving the direction of a moving target with single detector. Two detectors with in phase (I) and quadrature phase (Q) which is the real part and imaginary part of complex wave. The unwrapped phase of this set of complex numbers gives the information of the instantaneous direction of the target.

When the target fluctuates periodically, we can evaluate the fluctuation frequency from the radar output. This can be utilized for the measurement of vital signals as a non-contact method. An FM-CW radar is the most common in vehicle applications. However, the radar also utilizes the Doppler effect to determine the relative velocity between one's own car and the oncoming car or the receding car.

2.4. Spatial resolution in the azimuth (cross-range) direction

The spatial resolution in the range direction depends on the modulation bandwidth and pulse width as described in 2.1 and 2.2, respectively. In this section, the resolution in the azimuth (cross-range) direction is discussed. In a real aperture radar, the cross-range resolution corresponds to the beam width of a transmitted wave at the object position. As shown in Figure 2, the radiation pattern in the cross-range direction at the distance R is given by

$$W_A(x) = \left| \mathrm{sinc}\left(\frac{kD_A}{2R} x \right) \right|, \tag{12}$$

where k is the wavenumber of the transmitted wave ($k = 2\pi/\lambda$), and D_A is the aperture size of a radiation antenna. Since the halfwidth of the main lobe (half distance between first zero-crossing) of the *sinc* function is $2\pi R/kD_A = \lambda R/D_A$, the spatial resolution is evaluated as (Figure 2)

$$\Delta x \cong \lambda R/D_A. \tag{13}$$

This value becomes relatively large in a remote sensing, for example, $\Delta x = R\lambda/D_A = 100$ m for $\lambda = 2$ cm, $R = 1000$ m, and $D_A = 20$ cm. In order to obtain the resolution of $\Delta x < 1$ m, the required antenna size becomes larger than 20 m, which is rather impractical.

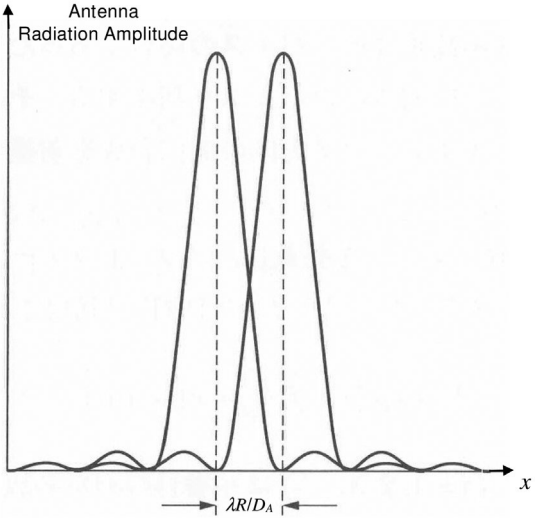

Figure 2. Antenna radiation pattern in the cross-range direction at the object point. The halfwidth of the main lobe (half distance between first zero-crossing) of the *sinc* function is $2\pi R/kD_A = \lambda R/D_A$. The resolution of real aperture radar depends on the beamwidth.

3. Application to plasma diagnostics

3.1. Plasma reflectometry

Reflectometry is expected to be one of the key diagnostics to measure density and density/magnetic-field fluctuations in large fusion devices. When an electromagnetic wave is launched into a plasma as shown in Figure 3, the wave is reflected at the corresponding cut-off layer. The microwave beam in the plasma undergoes a phase shift with respect to the reference beam. This phase difference as a function of the probing frequency is given by

$$\phi(\omega) = 2k \int_{a}^{r_c(\omega)} N(r,\omega)dr - \frac{\pi}{2} \tag{14}$$

within the WKB approximation, where k and ω are the wavenumber and frequency of the probing beam, N is the plasma refractive index, and a and $r_c(\omega)$ are the plasma and the cut-off radii, respectively. The refractive index of the ordinary (O) mode and the extraordinary (X) mode propagations are given by

$$N_O = \sqrt{\varepsilon_O} = \left(1 - \frac{\omega_{pe}^2}{\omega^2}\right)^{1/2} \tag{15}$$

$$N_X = \sqrt{\varepsilon_X} = \left(1 - \frac{\omega_{pe}^2}{\omega^2} \cdot \frac{\omega^2 - \omega_{pe}^2}{\omega^2 - \omega_{pe}^2 - \omega_{ce}^2}\right)^{1/2}, \tag{16}$$

where c is the speed of light, ε_O and ε_X are the plasma permittivity, and ω_{pe} and ω_{ce} are the electron plasma frequency and the electron cyclotron frequency, respectively.

The cut-off frequency determined from $N_O, N_X = 0$ is given by

$$\omega = \omega_{pe,} \quad \omega = \pm\frac{\omega_{pe}}{2} + \frac{1}{2}\left(\omega_{ce}^2 + 4\omega_{pe}^2\right)^{1/2} \tag{17}$$

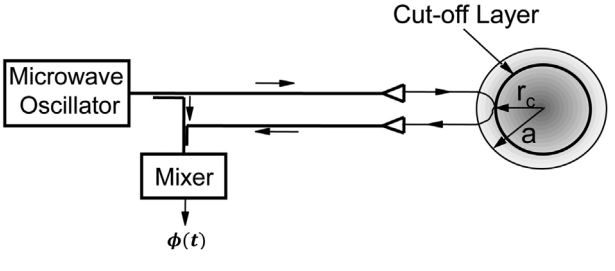

Figure 3. Schematic of the reflectometer configuration for plasma diagnostics.

in the cold plasma approximation. For the *O*-mode propagation, this integral can be analytically solved for the density profile using, for example, an Abel inversion. For the *X*-mode propagation, a numerical algorithm has been developed to invert the data [2–7]. One of the most serious problems in density profile measurement using conventional FM-CW reflectometry is caused by the existence of density fluctuations in plasmas, since the multi-fringe phase changes produced by a reflectometer are easily masked by those due to the density fluctuations. Several methods have been investigated to avoid this problem such as an ultrafast-sweep FM reflectometry, an amplitude–modulation (AM) or dual-frequency differential reflectometry and pulse-radar reflectometry as well as advanced data processing techniques based on a sliding fast Fourier transform (SFFT) algorithm, and on the wavelet transform or the maximum entropy method [3,8–13].

Reflectometry has also been used to study plasma fluctuations, since fluctuation-induced transport is considered to be one of the major problems for magnetic confinement plasmas. Consider that the permittivity varies in the direction of the signal propagation as

$$\varepsilon(r) = \bar{\varepsilon}(r) + \delta\varepsilon(r), \tag{18}$$

where $\bar{\varepsilon}$ is the average value of the permittivity, and $\delta\varepsilon$ is the fluctuation component due to density fluctuations. These fluctuations result in phase fluctuations given by

$$\delta\phi = k_0 \int_a^{r_c} \frac{\delta\varepsilon(r)}{\sqrt{\bar{\varepsilon}(r)}} dr. \tag{19}$$

The phase of the received signal is strongly affected by the fluctuations near the cut-off layer ($\bar{\varepsilon} \cong 0$), while the amplitude remains almost the same, which corresponds to the phase screen model [14].

Reflectometry has become a common diagnostic technique in fusion oriented magnetic confinement devices [15–20]. In fluctuation diagnostics of plasmas, the important issues are to obtain wavenumber resolved information as well as temporally and spatially resolved ones. Due to this point of view, radial and poloidal correlation reflectometry [21,22] and Doppler reflectometry which uses an oblique microwave beam and picks up the backscattered signal [23,24] have been applied to the measurements. In order to perform localized fluctuation measurements over a wide range of radial positions, an ultrafast sweeping source [25] or a comb generator source [26] are often utilized as well as one or two fixed frequency sources, since the fluctuations are 'frozen' during the measurement time.

Fluctuation-induced transport continues to be a serious problem in magnetically confined plasmas and its study is well suited to reflectometry. The dynamic behaviors of density/magnetic fluctuations during the L to H transition [27,28], the fluctuation spectra of edge localized modes (ELMs) [20,29], and fluctuations over the whole plasma radius from the scrape-off layer (SOL) to the core have been measured using various types of reflectometry [25,30].

3.2. Imaging reflectometry

3.2.1. Motivation

In microwave reflectometry of plasmas, the WKB approximation is often used for interpretation of received signals. According to this approximation, density fluctuations are supposed to affect the phase of a probing signal, and do not change its amplitude. Therefore, near the cut-off region, the shape of the signal wavefront corresponds to the shape of the fluctuations. If the variation of the density fluctuations is small or the width of their wavenumber spectrum is narrow, the microwaves bear phase information on a large distance, and interpretation of the signal is straightforward. Otherwise, interference of the scattered wavefront destructs the shape of phase close to the cut-off position, thus making difficult extraction of the information from the reflectometer signal. One of the possible ways to solve this problem is microwave imaging reflectometry (MIR) [31–33].

There exists two-types of schemes in MIR. One is synthetic aperture imaging and the other is optical imaging. The synthetic aperture imaging approach consists of a transmitting antenna and an array of receiving antennas. The signal reflected at a local point arrives at each of the antennas at a different time depending on the direction of the source. The Fresnel–Huygens formula is utilized in order to reconstruct the phase changes due to fluctuations at the cut-off layer [34,35]. The optical imaging approach uses large aperture optics to restore the wavefront at the receiver position [36,37]. In this paper, we describe the latter case, that is, optical imaging.

3.2.2. System development

Pioneering tests of the MIR concept were conducted by Munsat *et al.* with a proof-of-principle system implemented on the TEXTOR tokamak [36]. In order to assess the efficacy and limitations of the MIR concept, they performed simulations, laboratory tests, and both plasma and test object evaluations of the TEXTOR prototype system. Initial experiments on TEXTOR demonstrated the promise of MIR and produced a number of interesting physics results such as poloidal rotation reversal after neutral-beam injection is turned off. However, many features of the raw data bore the characteristic deleterious symptoms of standard reflectometry, which arose from misalignment of the MIR system. Due to the nature of the optical system designed to match the small circular curvature of the TEXTOR plasma, a problem that was significantly alleviated on the follow-on DIII-D system, optical alignment was extremely sensitive.

The position of transmitting and receiving point and distance between lenses/mirrors are determined from the accessibility condition to the machine. The focusing point or the wavefront at the cut-off layer is determined from the plasma shape. The optics design is characterized using a ray tracing code, such as, Code V and Zemax and FDTD (finite difference time domain) simulation code [36–39]. Figure 4 shows the propagation behavior of incident, reflected, and local oscillator waves using an FDTD code for the LHD (large helical device) plasma [38,39]. The

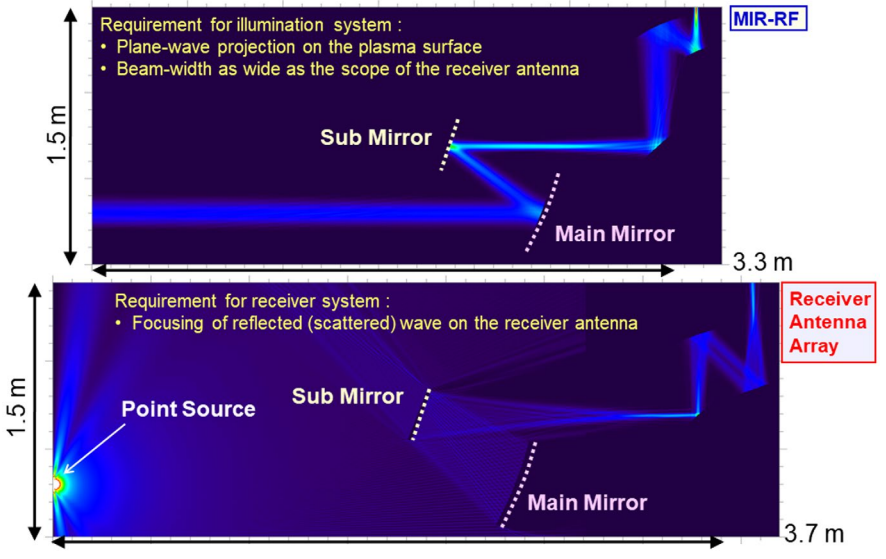

Figure 4. The behaviors of transmitting wave (upper figure) and reflected wave (lower figure) calculated using FDTD simulation code. The ellipsoidal or hyperboloidal surfaces of the curved aluminum alloy mirrors (main mirror and sub-mirror, respectively) were installed in a vacuum chamber of LHD for simultaneous focusing of the transmitting and receiving components.

ellipsoidal or hyperboloidal surfaces of the curved aluminum alloy mirrors were installed in a vacuum chamber of LHD for simultaneous focusing of the components (the illumination wave, the reflected wave, and the LO wave). The UC Davis Group has also investigated the utilization of electronically controlling zooming optics to match the wavefront with curvature of the cut-off layer corresponding to the multi-frequency incident sources. [40,41].

Figure 5 schematically illustrates the DIII-D MIR system [41,42], which is an extension to two-dimensional (2-D) with 12 vertically separated sightlines and four-frequency operation (corresponding to four radial channels). Features that distinguish the 48-channel DIII-D MIR system are: (i) illumination frequencies that can be tuned within 500 μs over a range of 56 to 74 GHz, (ii) an innovative optical design that keeps both on-axis and off-axis channels focused at the cut-off surface, and (iii) shared port with electron cyclotron emission imaging (ECEI), thereby permitting simultaneous measurements of electron temperature and density in the same volume of plasma. These key features permit visualization and quantitative diagnosis of density perturbations, including correlation length, wavenumber, fluctuation velocities, and dispersion.

The MIR instrument usually uses a heterodyne receiver to obtain an intermediate frequency (IF) signal. One of the important issues is to supply sufficient LO power (1–10 mW) to a mixer to achieve low conversion loss for good signal to noise ratio. In the conventional MIR, the LO power is also fed quasi-optically to a mixer together with reflected signals using focusing optics. However, it is rather

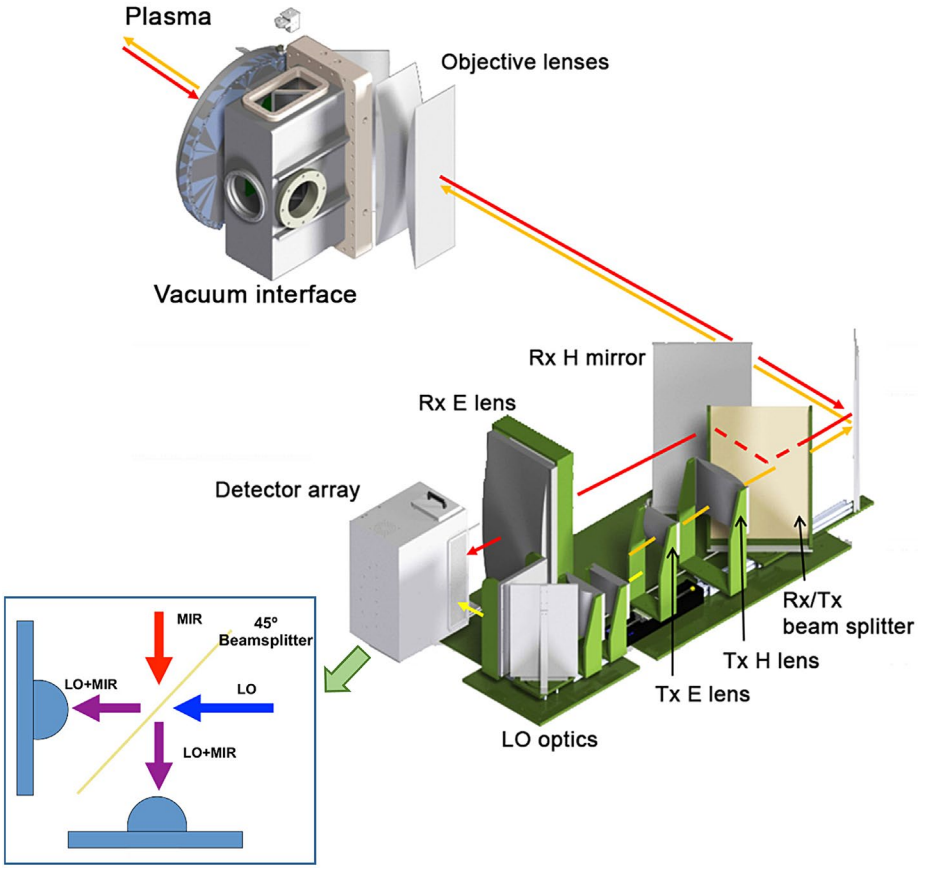

Figure 5. Computer model of the DIII-D MIR configuration. The transmit (Tx), receive (Rx), and local oscillator (LO) beam paths are shown in orange, red, and yellow, respectively. The reflected wave and the reference wave are combined to obtain the down-converted intermediate frequency wave using a beam splitter. (from Ref. [42]). Copyright 2014 AIP Publishing.

difficult to uniformly irradiate LO power on an array detector depending on the array size. Figure 6 shows an example of the power profile of the probe beam, which is measured by a power monitor with a V-band pyramidal horn antenna [43]. The spot size of the probe beam is 20 cm vertically and 15 cm horizontally at $z = 0$ cm, and the spot size varies a few cm between $z = -40$ and + 40 cm. Here, z is the distance from the focal plane. The illumination wave is a parallel beam with a diameter of 20 cm in the observed region. As is readily apparent, the uniformity of the LO power level is not satisfied.

Both a conventional system and a new MIR system are depicted in Figure 7. Figure 7(a) shows that both the RF wave (reflected wave) and LO wave enter an array detector. In order to provide sufficient LO power to each channel, the LO power should be very high, and this increases the cost of the system. Figure 7(b) shows a new system, which uses the technology to combine waveguide and microstrip line for heterodyne detection radiometer. This device is called the horn-antenna

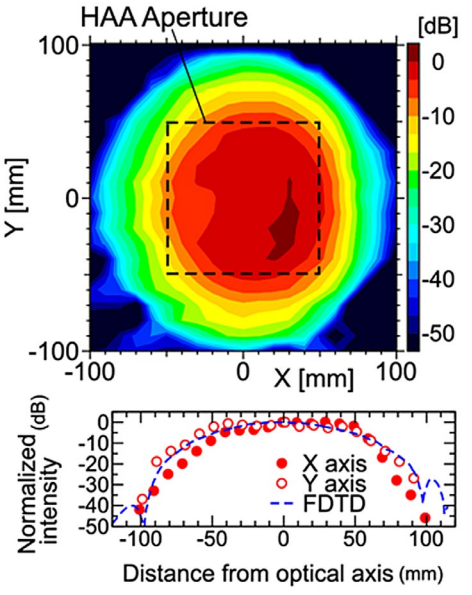

Figure 6. Radiation pattern of the LO beam at the detector (mixer) position. (from Ref. [39]). Copyright 2010 The Japan Society of Plasma Science and Nuclear Fusion Research.

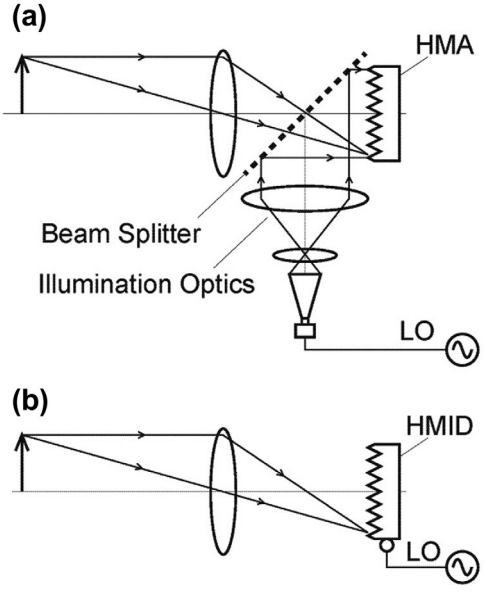

Figure 7. The feeding method of LO: (a) conventional method, (b) new method (from Ref. [47]). Copyright 2017 AIP Publishing.

millimeter imaging device (HMID) using a local-integrated array (LIA). A schematic of each HMID channel is shown in Figure 8. In the HMID, the RF wave is transmitted from the waveguide to the microstrip line using a finline transmitter, and the LO power is delivered by coaxial cables. Since the LO optics are not

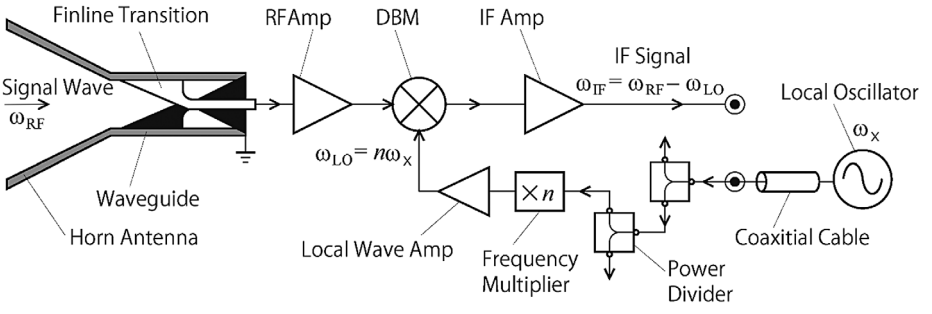

Figure 8. Schematic of the horn-antenna millimeter-wave imaging device (HMID).

required, the imaging optics become significantly simplified in this MIR system. With the incorporation of a low-noise amplifier (LNA) in the front-end of the heterodyne detection, the signal-to-noise ratio (S/N) can be significantly improved. The finline transmitter enables installation of the front-end LNA in the HMID.

Figure 9 shows an assembly drawing of a 2 channel LIA [44,45]. The LIA consists of 6 important elements: horn antennas, waveguides (WG) to microstrip line (MSL) transmission, mixer, LO module, LO power divider, and IF transmission line. Horn antennas and WG to MSL transmission consist of a sandwich with a high-frequency printed circuit board (PCB) placed between the upper and lower aluminum frames, which engraved one-half of horn antennas and waveguide shapes. The receiving wave (RF) enters the mixer via a horn antenna and a WG to MSL transmission, and it converts the IF signal (110 MHz) by the use of the LO wave (60 GHz) generated by the quadrupler. Pre-LO signals (15 GHz) are supplied to each quadrupler by a power divider using a Wilkinson power divider method. Since the LO power divider is installed between the mixer and an output connecter, IF signals have to stride over a transmission line. With the incorporation of a low noise amplifier (LNA) in the front-end of the heterodyne detection,

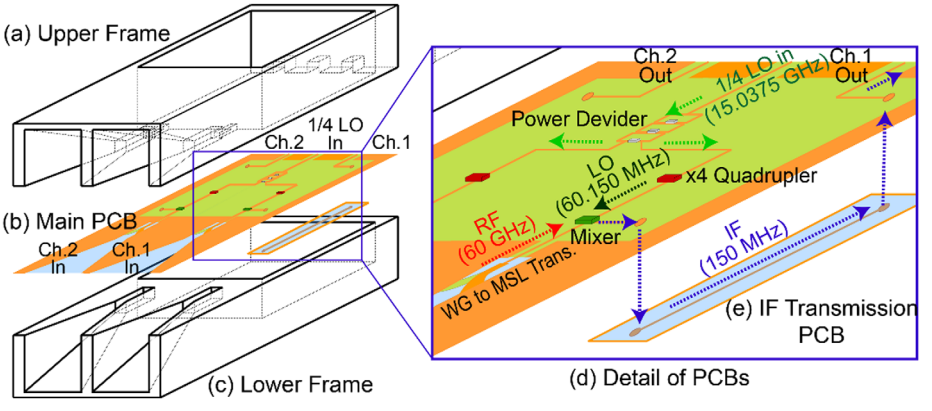

Figure 9. Assembly drawing of local integrated array (from Ref. [45]). Copyright 2015 IOP Publishing.

the signal-to-noise ratio can be significantly improved. The finline transmitter enables installing the front-end LNA in the HMID. In the early stage of experiment, reflected waves from the cut-off surfaces corresponding to each frequency are focused via the imaging optics onto an aperture of 2-D horn antenna array (HAA) with mixers. The array consists of 35 small horns aligned in toroidally 5 by poloidally 7 channels.

3.2.3. Application to magnetically confined plasmas

In comparing MIR to other systems, it performs well as a density fluctuation diagnostic. Spectral features measured by other independent density diagnostics, such as interferometry and beam-emission spectroscopy, are also strong in the MIR spectrum. A high-confinement discharge on DIII-D with edge localized modes (ELMs) is presented here to demonstrate some of MIR's capabilities. Inter-ELM density fluctuations, such as the upward sweeping modes, are clearly seen from interferometry as well as with the MIR instrument (compare Figure 10(a) and (d)). The core-localized tearing mode at 70 kHz produces a prominent magnetic fluctuation (Figure 10(c)) but is not strong from the perspective of electron cyclotron

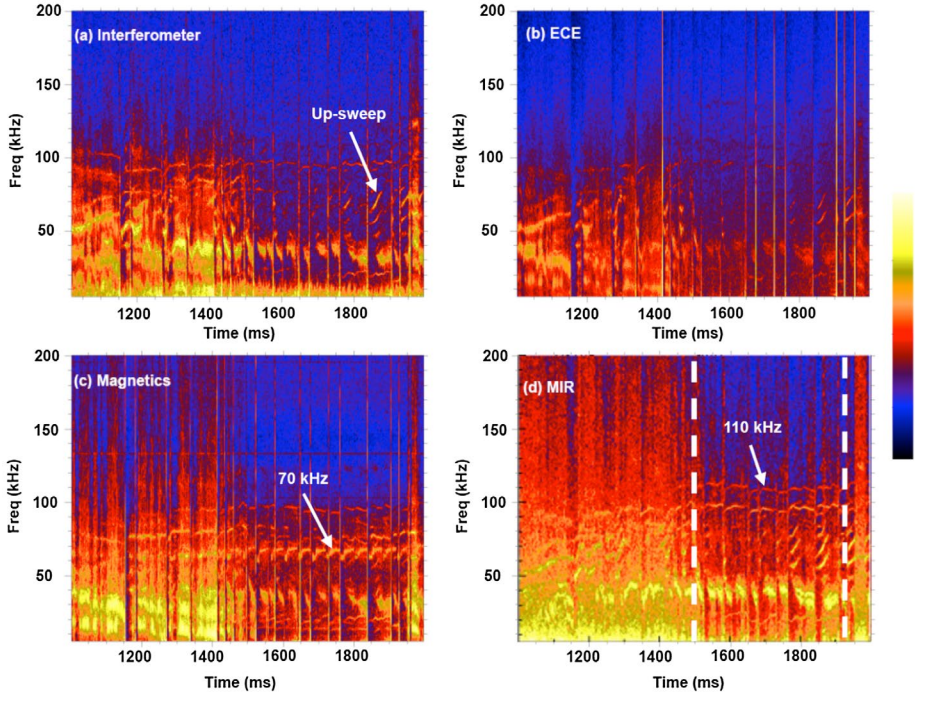

Figure 10. Spectrograms of (a) cross-power between radial and vertical interferometer chords (frequency sweeping mode activity is indicated), (b) cross-power between two ECE channels located just inside the last-closed flux surface, (c) cross-power between two high-frequency magnetic coils located outside the plasma and near the mid-plane (core mode uniquely observed on magnetics is indicated), and (d) autopower of a representative MIR channel (the 110 kHz mode uniquely observed on MIR is indicated). The region between the vertical dashed lines indicates times where the best focusing is achieved with MIR.

emission (ECE), interferometry, or MIR. Each diagnostic detects a coherent fluctuation at 100 kHz, but MIR also readily detects a neighboring mode at 110 kHz (Figure 8(d)), which is near the noise level in the other diagnostics. One possible explanation for the clear signature on MIR is that its high sensitivity to small density perturbations and its highly localized spatial measurement allows MIR to detect fluctuations that line-averaged measurements (such as interferometry) and external measurements (such as Mirnov coils) cannot.

MIR produces a local measurement so that mode amplitude and phase structure may be reconstructed across a 2-D cross-section of the tokamak plasma. Numerous inter-ELM modes are simultaneously imaged over the same plasma volume. Each ELM burst precedes a set of coherent modes that sweep upward in frequency (see Figure 11). The arrows indicate ELMs. Following an ELM, a set of coherent modes appears at 55, 65, and 75 kHz, and they sweep in frequency over time. A difference of approximately 10 kHz is maintained between the modes. The mode amplitude peaks around 1/4th the ELM period, and fades below the noise floor about 1/3rd the ELM period.

Images of the mode at 1778 ms and 58 kHz (boxed in Figure 11) are produced by Fourier transforming the measured fluctuation signal from each of the 48 MIR channels. A time window centered at 1778 ms for each channel is Fourier-transformed and the spectrum at 58 kHz is integrated with 1 kHz averaging window. The integrated amplitude is recorded for each channel and plotted on a 2-D grid corresponding to radius (R) versus elevation (z) in the tokamak plasma. The resulting image of the 58 kHz fluctuation is shown in Figure 10. The series of panels on the right represent a time sequence of the density fluctuation measured by MIR (top) and temperature fluctuation measured by ECEI (bottom), where each panel represents 1/8th of the period of the mode. In the left panel of Figure 12, the last-closed flux surface (LCFS) of the plasma is mapped to spatial coordinates using an equilibrium reconstruction constrained by external and internal magnetic diagnostics. The plasma region measured by MIR (region boxed in blue) is determined by calculating the right-hand X-mode cut-offs for the four

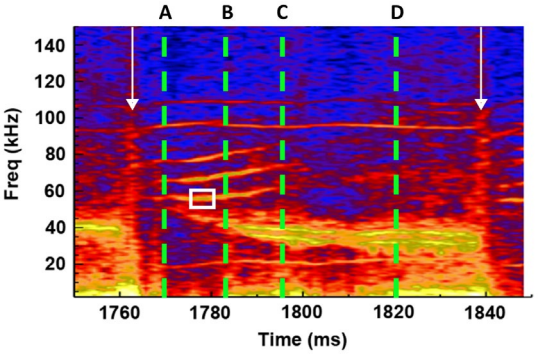

Figure 11. MIR autospectrum of one representative channel showing two ELM bursts (denoted as vertical arrows) and inter-ELM activity. The box encircles the 58 kHz mode at 1778 ms.

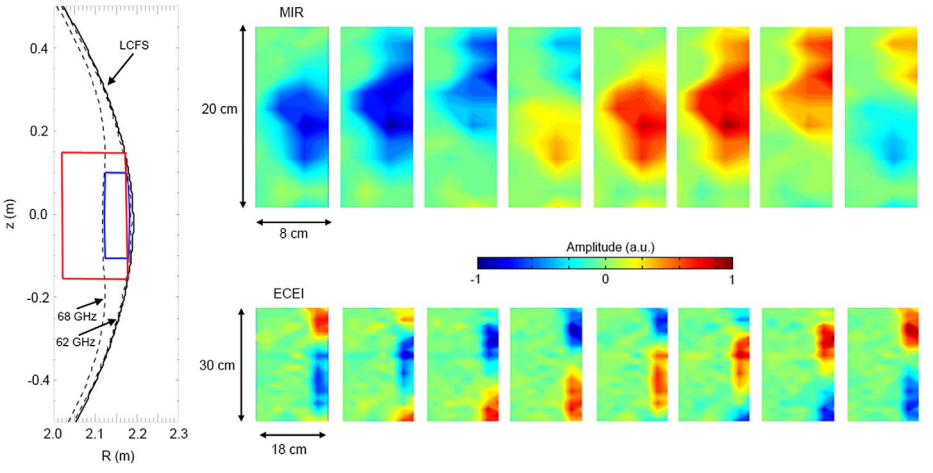

Figure 12. (a) Mapping of the two-dimensional coverage areas measured by MIR and ECEI onto a poloidal-radial cross-section of the DIII-D plasma. The smaller of the two boxes is the MIR window. The cut-off layers are calculated by the cold plasma dispersion relation including a relativistic correction to the electron mass. The cut-off layers corresponding to the highest and lowest MIR probe frequencies used for this particular discharge are overplotted, as well as the last-closed flux surface (LCFS). (b) Time sequence of the 58 kHz density fluctuation at 1864 ms measured by MIR (top) and temperature fluctuation measured by ECEI (bottom).

probe frequencies used in this experiment (62, 63, 67, and 68 GHz). The region measured by ECEI is boxed in red.

Its 2-D measurement capability and high time resolution (0.5 μsec depends on the detector bandwidth and sampling time of a digitizer) allows MIR to quantify dynamic properties of density fluctuations, namely local values of the phase and group velocity. Complementing the frequency–time domain spectrograms (such as those in Figures 10 and 11), frequency–wavenumber dispersion maps offer an extra dimension to the data. While spectrograms illustrate the power distribution in frequency and time, dispersion maps reveal the power distribution in frequency and wavenumber, from which group and phase velocities can be inferred. A four-panel time sequence of the density fluctuations measured by MIR from Figure 11 is shown in the frequency–wavenumber domain in Figure 13. The data are taken at the 63 GHz cut-off layer located in the steep gradient region of the pedestal.

Coupled modes and broadband turbulence form a relationship in the frequency–wavenumber domain from which their group velocity can be determined. Oftentimes it is observed that groups of modes and turbulence form a linear relationship from which the group velocity is approximated.

An example of this type of analysis is applied to the data shown in Figures 11–13. The time within the ELM period from which each dispersion map in Figure 13 is generated is indicated by a vertical dashed line on the spectrogram in Figure 11. Early in the ELM period, appreciable power grows in at least three distinct high-frequency spectral components (f ~ 55, 65, and 75 kHz) and from frame A of Figure 13, it can be seen that they form a linear relationship with a

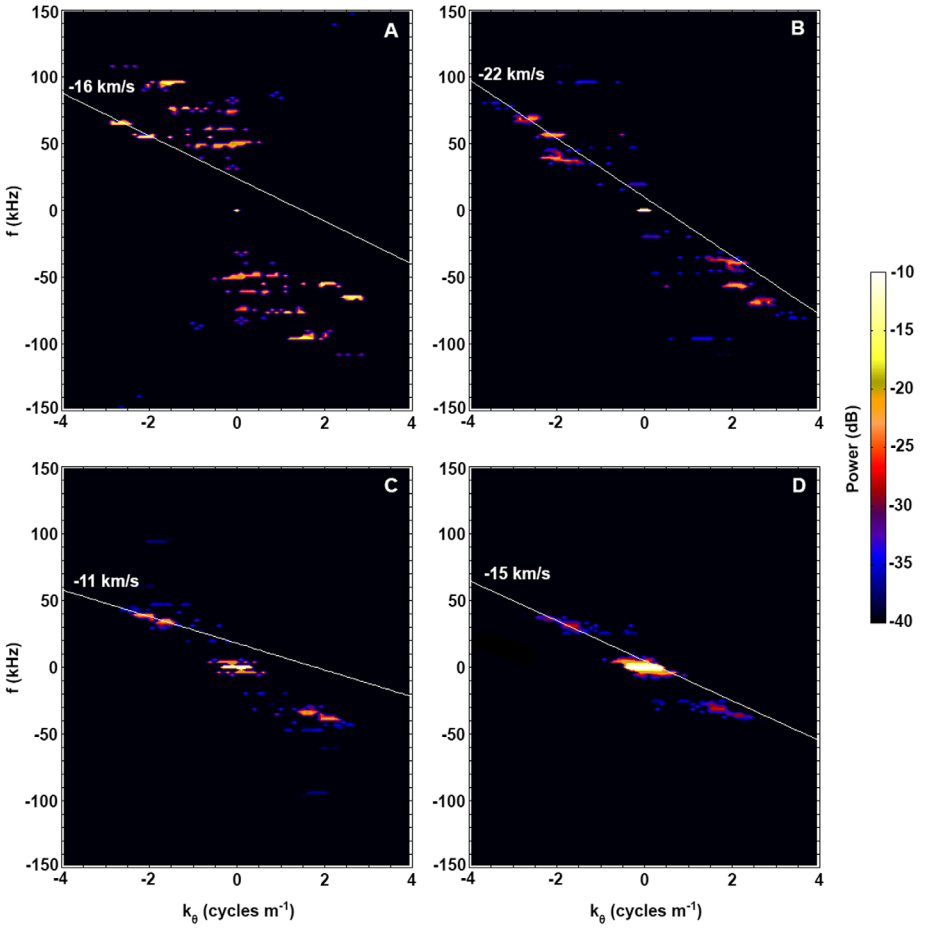

Figure 13. Dispersion maps of density fluctuations measured by MIR in the pedestal between the two ELMs shown in Figure 4. The letters of each panel correspond to the times denoted by the vertical lines in Figure 4.

group velocity of −16 km/s. By frame B, power grows in a number of additional modes, and the three high-frequency modes seen in frame A persist, sweeping up slightly in frequency. A linear fit to the high-frequency set of modes in frame B yields a group velocity of −22 km/s. About 1/3rd through the ELM period, the high-frequency modes disappear, and power grows substantially in a lower frequency pair of modes as well as a low-frequency broadband feature. These two sets of fluctuations persist until the onset of the next ELM.

An O-mode MIR is applied to LHD plasmas [46,47]. The edge density fluctuation is measured in L-mode and H-mode plasmas. The key parameters of fluctuation are the wave number (k) and the frequency (ω). In order to obtain the k-ω spectrum two-point cross-spectrum $S_{ij}(\omega)$ is evaluated [46]. The wave numbers between two MIR channels (i, j) which have the distance of d_{ij} can be obtained from

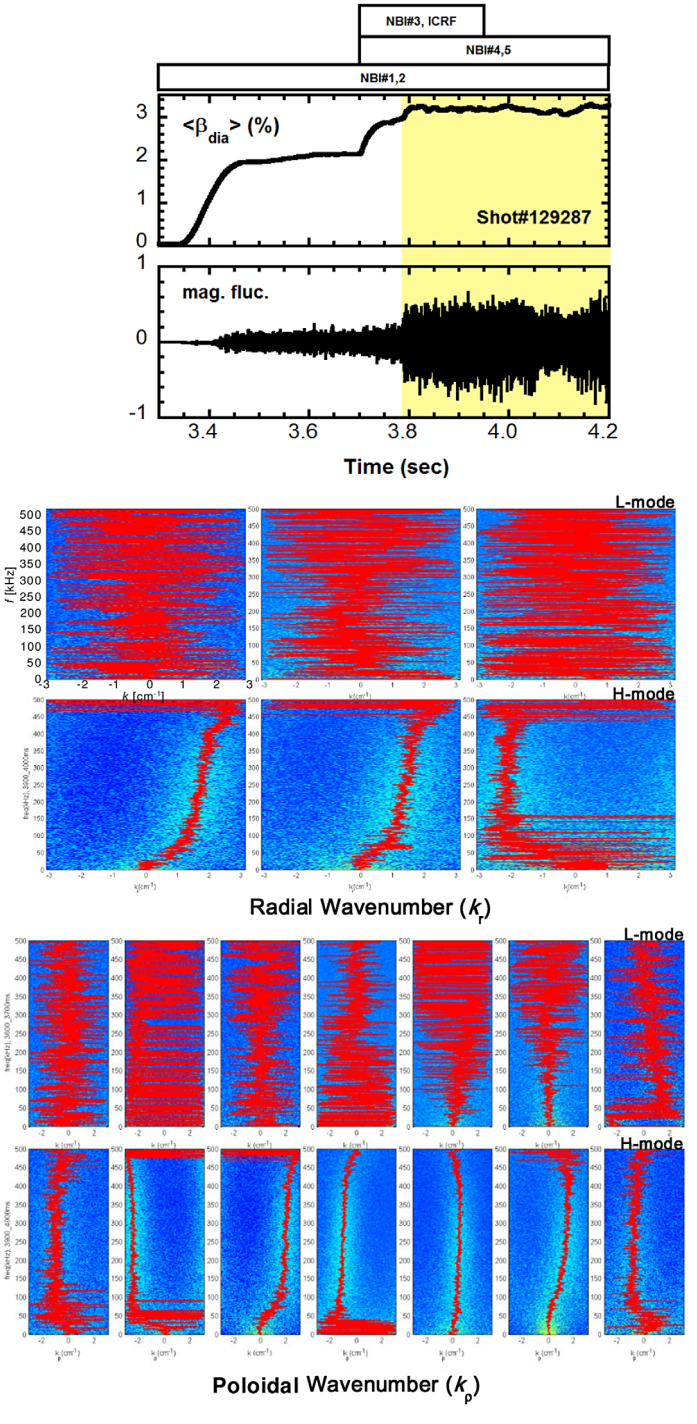

Figure 14. The *k*-ω spectra of the fluctuations obtained by MIR during L-mode to H-mode transition.

$$k_{ij} = \frac{1}{d_{ij}} \tan^{-1}\left(\frac{\mathrm{Im}S_{ij}(\omega)}{\mathrm{Re}S_{ij}(\omega)} \right). \tag{20}$$

The coherence is the normalized cross-power spectrum given by

$$\mathrm{coh}_{ij}^2(\omega) = \frac{S_{ij}(\omega)}{S_{ii}(\omega)S_{jj}(\omega)}. \tag{21}$$

An example of the results is shown in Figure 14. Instability shows that a localized fluctuation burst is observed on the edge plasma in LHD. It is seen that a clear correlation is observed in the poloidal direction in the H-mode plasma.

MIR systems have been applied to various magnetically confined plasmas in the world such as DIII-D, LHD, KSTAR, ASDEX-U, and EAST, and produces useful information regarding fluctuations [48–51].

4. Application to biological signals

4.1. Fluctuation reflectometry for vital signal detection

4.1.1. Motivation

It is said that a considerable percentage of the world's population suffers from chronic diseases such as asthma, diabetes, or heart diseases [52–54]. The healthcare and monitoring are becoming increasingly important. Heartbeat signal is a very useful parameter for such monitoring. Several methods have been developed such as conventional electrocardiogram (ECG), piezo-electric sensor, ultrasonic sensor, infrared sensor, and microwave reflectometry sensor. Microwave reflectometry measures remotely the human skin and internal organs movements when breathing and heartbeat are present rather than the electrical impulses measured by ECG [55–60].

The heartbeat interval is constantly fluctuating by autonomous nerve activity comprised of sympathetic and parasympathetic nerve activity. The time variation can be regarded as the short-term time variation of the heartbeat frequency, the so-called heart rate variability (HRV). The HRV is obtained by interpreting the R–R intervals in an ECG data, where R is a point corresponding to the peak of the ECG, and R–R is the interval between successive Rs. In the frequency spectrum of the HRV, the parasympathetic nerve activity appears in the spectral region of 0.15–0.45 Hz (the so-called HF region), and both sympathetic and parasympathetic nerve activity appears in the region of 0.03–0.15 Hz (the so-called LF region) [61–66]. The peak ratio or area ratio of the power spectrum in the LF component to the HF component is used to evaluate the stress condition. The sympathetic nerve activity increases in a stressful state and the parasympathetic nerve activity increases in a relaxed state. The ratio LF/HF in a stressful state is larger than that in a relaxed state. The coefficient of variation of R–R intervals (CVRR) can also be

introduced as one of the indices to evaluate autonomous nerve activity. Combining these indices (time variation of HR, CVRR, and frequency spectra of HRV), the human mental and physical conditions can be evaluated with reliability [67–69].

Conventional electrocardiographic (ECG) monitoring has been a major tool for evaluating HRV. However, the evaluation method using the ECG seems to be unsuitable as a long-time monitoring subject, since several electrodes are attached directly to the human body to acquire the ECG data. Specifically, there is some concern about the practical application of the ECG system to sick persons and elderly persons. We propose microwave reflectometry as an HRV evaluation method since it is completely noninvasive and feasible even through thick clothing [70].

4.1.2. Apparatus for heart rate (HR) measurement

A heterodyne-type reflectometer as shown in Figure 15 is applied to the initial experiment. A microwave oscillator with frequency of 10 GHz is used as an incident wave and a local oscillator (LO) wave. One of the waves passing through a directional coupler is shifted by the signal from a VHF oscillator with frequency of 110 MHz using a single-sideband up-converter, which is irradiated onto the area near the human heart or the path of an artery in the thigh via a $1 \times 2 \sim 2 \times 4$ element patch antenna array. The directivity of antennas is selected depending on the position of the HR measurement. High gain antennas are needed in the case of remote measurement (>1 m) irradiating the vicinity near the heart from the chest front. However, rather low gain antennas are preferable for the short distance measurement (<10 cm) such as the thigh back side. Since the phase fluctuation has to be analyzed rather than the amplitude of the reflected wave,

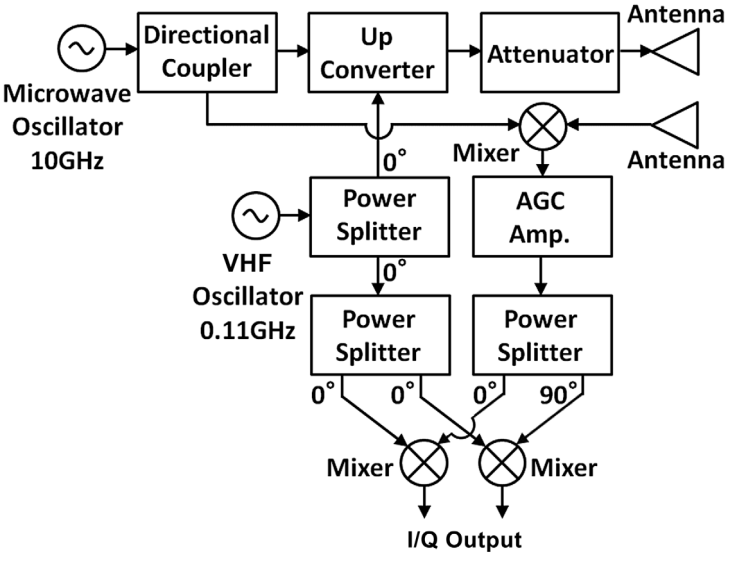

Figure 15. Schematic of the heterodyne reflectometry with an AGC amplifier.

Table 1. Attenuation constant and skin depth in the body tissues for various frequencies.

			Attenuation Constant α (cm^{-1})			Skin Depth δ (cm)		
Body Tissue	ε_r	ε_i	24 GHz	10 GHz	1 GHz	24 GHz	10 GHz	1 GHz
Fat	4.8	1	0.92	0.38	0.038	1.1	2.6	26
Heart	47	21	6.1	2.5	0.25	0.16	0.40	4.0
Muscle	40	18.5	7.2	3.0	0.30	0.14	0.33	3.3
Blood	50.4	23	7.9	3.3	0.33	0.13	0.30	3.0

Notes: ε_r: Real part of complex relative permittivity; ε_i: Imaginary part of complex relative permittivity.

the optical alignment of radiation beam is not important so long as a sufficient signal to noise ratio is observed.

The reflected wave from the skin and the surface of the heart is picked up by another identical antenna, and down-converted to an intermediate frequency (IF) signal of 110 MHz. An automatic gain control (AGC) amplifier with frequency range of 100–200 MHz is utilized to control the reflected wave in both static and non-static environments. The quadrature phase detector provides two components in the mixer output, $E_rE_l\cos\Delta\varphi$ and $E_rE_l\sin\Delta\varphi$, where E_r and E_l are the amplitude of the reflected wave and the local oscillator wave, respectively, and $\Delta\varphi$ is the phase difference between the reflected wave and the local oscillator wave. We can distinguish the amplitude and the phase difference of the reflectometer signals by detecting the above two components. The AC components of the phase difference include the periodic movement of the reflection layer due to the heart beat as well as the random movements of the human body [71]. In order to discuss the reflection layer, the skin depth of the electromagnetic waves is calculated for frequencies of 1, 10, and 24 GHz in Table 1. Here the complex permittivity is assumed to be almost constant from 1 to 24 GHz [72]. The reflected waves primarily come from skin layer at the frequency larger than 10 GHz.

To extract the heartbeat signal from the measured signal, for example, the respiration signal is removed by a high-pass filter with a cut-off frequency of 0.7 Hz. The spurious component of the reflected wave due to random movement of the human subject is difficult to remove, since it has a wide frequency spectrum. Additionally, the heartbeat signal is very small and has a low signal-to-noise ratio, because the cardiac movement appears on the body surface through the bone and the connective tissue. Thus, the peak positions in the heartbeat signal obtained by a microwave reflectometer are not as clear as those observed in the ECG signals, which makes it difficult to infer the heart rate correctly by interpreting the peak intervals of the microwave measurement signal without any data processing.

4.1.3. Signal processing for evaluation of heart rate variability (HRV)

The heart-rate measurement by a microwave reflectometer is applied to a person who is in a static or a non-static environment. In the non-static environment, the microwave reflectometer signal includes various fluctuation noise due to random movement of the body surface, thus making it more difficult to detect the heartbeat interval corresponding to the R–R interval of ECG signals. Figure 16 shows an

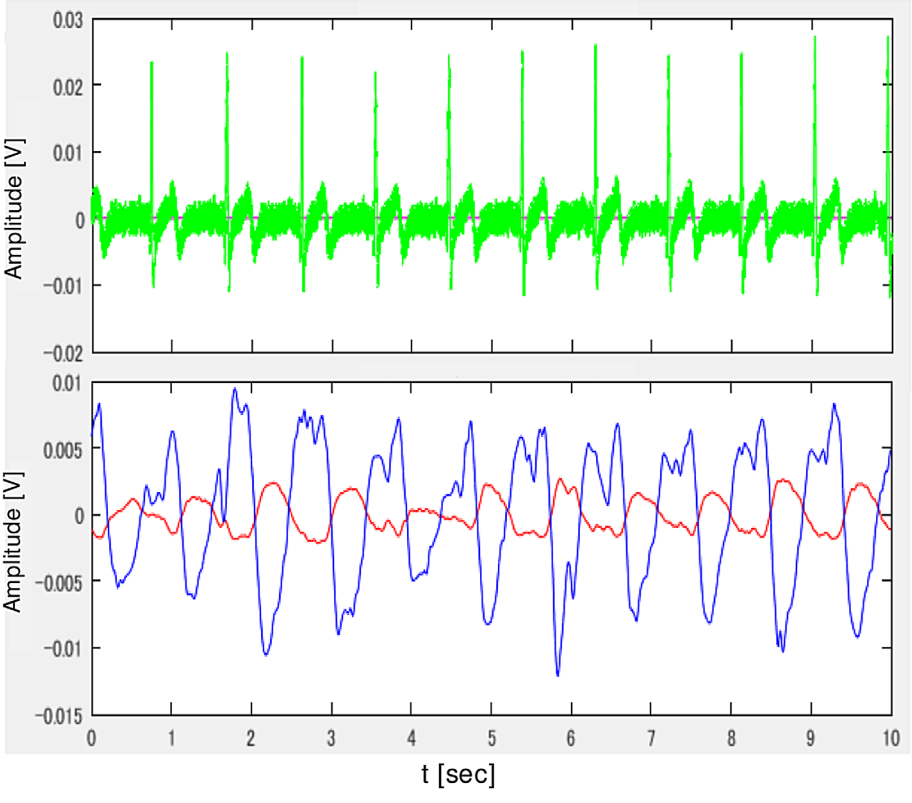

Figure 16. Comparison between ECG signal (upper) and microwave reflectometer signals (lower).

example of the measurement for a person sitting on a chair at his desk together with an ECG data. Microwave reflectometers measure two positions under the thigh. Two sets of antennas are buried in the seat pad of the chair. It is advantageous to irradiate a microwave near the heart in order to obtain enough heartbeat signals. However, the evaluation of the HRV becomes extremely difficult since much bigger phase fluctuations due to respiratory movement are mixed. Note that the detection of peak (R–R) intervals in an ECG signal is simple. However, this is rather difficult in a microwave signal. Two novel methods (algorithms) are proposed to evaluate heartbeat intervals clearly [73,74].

4.1.3.1. Template and cross-correlation algorithm. In this algorithm, a template signal is formed by the arithmetic average of a reflected wave. Then, the cross-correlation function between the template and the measurement signal is calculated to obtain a clear peak waveform for evaluation of R–R intervals. The steps of the process are as follows:

The peak positions of the synchronized signals with the heartbeat are picked up and selected in the range of ±30% of an assumed peak value. The waveforms are picked out in the time length of the selected peak positions ±0.5 s in series.

The extraction time length is selected appropriately depending upon the measurement conditions. In the present system, the heart rate is assumed to be in the range of 30–120 beats per minute (bpm). It is desired that the template signal contains characteristics of one heartbeat waveform. If the template signal does not contain characteristics of one heartbeat waveform, the peak intervals of the cross-correlation function waveform become unclear.

A span of 30–120 bpm sufficiently covers the heart rate for a human subject, since it is typically in the range of 45–90 bpm, i.e. 0.75–1.5 Hz [75,76]. Then, cross-correlation function between the template and the measurement signal is calculated. If any of the peak values in the cross-correlation function fall below 0.5, the cross-correlation functions are calculated repeatedly as the second or the third cross-correlation functions. This method works well for the case in which large noise components are mixed with the reflectometer signals which renders it difficult to identify the peak intervals in the first cross-correlation function. The HRV is obtained by interpreting the peak intervals in the cross-correlation function.

4.1.3.2. MEM algorithm. The time variation of the heartbeat frequency is evaluated by applying the maximum entropy method (MEM) repeatedly. The time window is shifted step by step along the temporal axis. Then, the HRV can be obtained since the value of the heartbeat interval is calculated by the inverse of the heartbeat frequency. The MEM is an effective application for estimating the frequency spectrum in a short data window.

In the MEM, the model order is generally unknown. If the model order is selected lower, the estimated spectrum is smoothed and the spectrum peak which should be found in a normal situation does not often appear. On the other hand, if the model order is selected higher, numerous spurious peaks appear finely in the estimated spectrum. The optimum selection of the model order is of importance in the MEM [77–79]. We have selected the optimum model order as 870 from empirically based experience.

The heartbeat frequency is estimated by finding the largest peak in the frequency range of 0.7–1.55 Hz (42–98 bpm) after calculating the power spectrum of some data windows by the MEM. Here, the frequency 0.7–1.55 Hz covers sufficiently the range of heartbeat frequency for a human subject. If the analyzing data window is selected long, time response of the heartbeat intervals becomes sluggish in the HRV while the reliability of the estimation increases. This could exert a bad influence upon the estimation of the LF/HF. In this paper, 2.5 s is selected as the optimum length of the data window for the MEM analysis from the empirically based experiences.

In addition, 0.25 s is selected as the shift quantity of the data window. This value is equal to the interpolated value of the HRV reconstructed by the ECG. Unlike the non-stationary spectrum analysis techniques, the MEM is highly regarded as a reliable stationary spectrum analysis technique where the consistency of the signal

in the data window is achieved. As the correspondence relationship between the data windows is ignored, some spectrum estimation errors due to the selected data window appear as the fluctuation with a period of 0.25 s, which is equivalent to 4 Hz of frequency in the HRV signal. This is not a difficulty for the evaluation of the stress, however, because the spectrum estimation error between data windows is very small and its fluctuation does not extend over the frequency region of the LF and the HF. For these reasons, the time variation of the heartbeat frequency is estimated by repeatedly applying the MEM at the 2.5 s data window which is then shifted by 0.25 s along the temporal axis.

4.1.4. Results of heart rate (HR) and heart rate variability (HRV)

The measurement and evaluation of HR and HRV are applied to a subject in both relaxed state and stressful state. Figure 17 shows an example of the measurement for a subject taking a flash calculation test [80,81]. In a flash calculation test a subject calculates a numerical problem displayed on a computer screen in sequence by mental arithmetic. During the time interval of 360–540 s, the person is taking a test. In another interval, 0–360 s and 540–900 s, the person is in a relaxed state. The algorithm based on the MEM made it possible to reconstruct the HRV correctly and automatically from low-S/N microwave reflectometer signals. The time–frequency spectrum of the MEM-based HRV data is obtained by the wavelet transform. Note that the HF components dominate in the relaxed state, while the LF components dominate in the stressful state.

The evaluation of LF/HF from HRV frequency spectra has been applied to 9 subjects under various conditions. The results are shown in Figure 18(a). The conditions given to the subjects are the following: 1 and 19 relax state, 3–6 flash

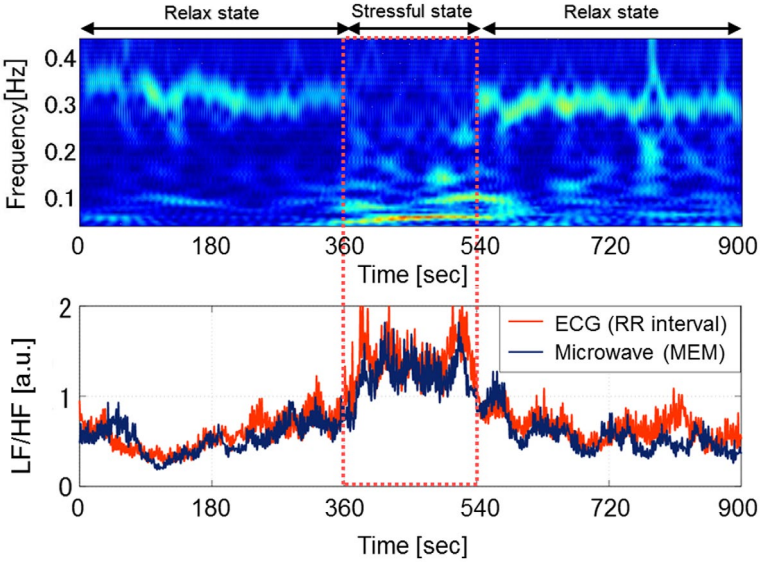

Figure 17. Wavelet spectrum of the HRV (upper trace), LF/HF as a function of time (lower trace).

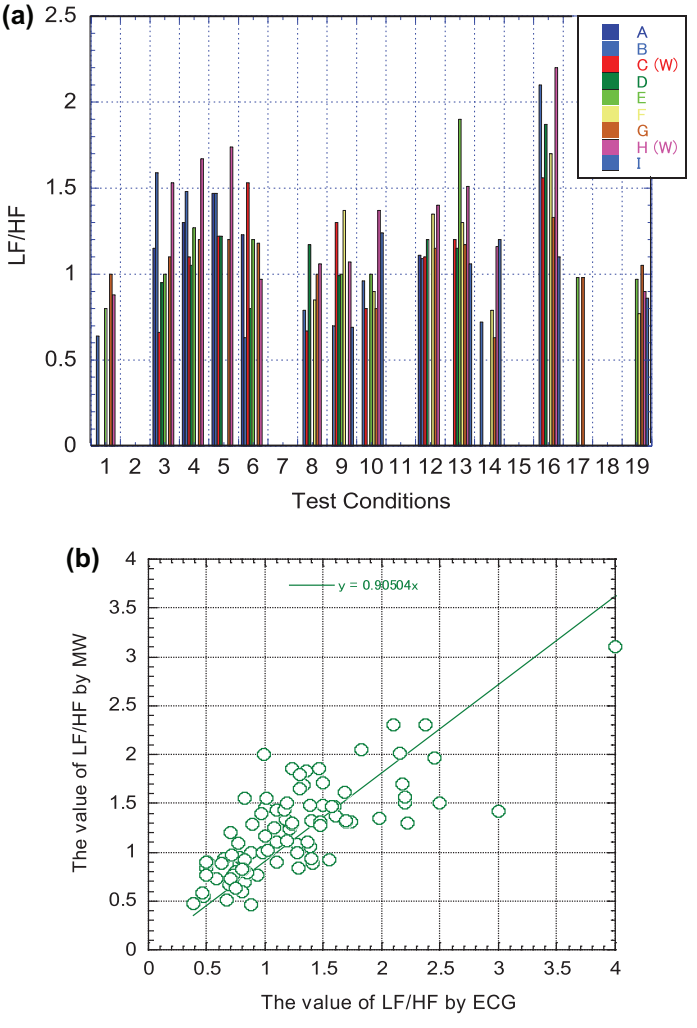

Figure 18. (a) LF/HF obtained for various conditions applied to 9 subjects (upper trace), (b) Comparison of LH/HF obtained by MW and ECG (lower trace).

calculation test, 8–10 listening to various music, 12–14 watching TV news of a natural disaster, and 16–17 ice test (physical stress). The subjects take a break between the test to reset the states, such as 2, 7, 11, 15, and 18. It is noted that there is a scattering in the LF/HF values depending on each individual [82]. However, the tendency is quite similar. The LF/HF values obtained by microwave reflectometry are compared with those obtained by ECG as shown in Figure 18(b). The agreement seems to be good (the correlation coefficient $r = 0.769$, the regression line $y = 0.90504x$) considering that the individual variability of LF/HF is said to be about ±30% [67,68].

The present system is also applied to the measurement of a driver's heart rate. It is known that a driver's physiological state is reflected by vital signals, such as heart rate, respiration, blood pressure, body temperature, and other factors.

Specifically, the heart rate variability can be used for the mental and physical states of drivers, and is considered to be useful for detecting drowsy driving and drunk driving. In the driving condition, the microwave measurement signal includes random and large body movements due to road noise and steering wheel control. A heterodyne-type I-Q phase detection system with an AGC amplifier as shown in Figure 15 is especially useful for these conditions.

The results are shown in Figure 19. The body movements due to vehicle run vibration often have similar periodicity to the heartbeat rhythm. It is therefore difficult not only to estimate the stress, but even to measure the heartbeat signal. We have succeeded in reducing the noise component and have extracted only the heartbeat signal by calculating a cross-correlation function between two measurement signals obtained from two microwave reflectometers [83]. The success rate of the heart-rate measurement by reflectometers is 70–80%. The success rate means the ratio of the measurement time to the term, in which the error of time variations of the heart rate is kept within ±10%.

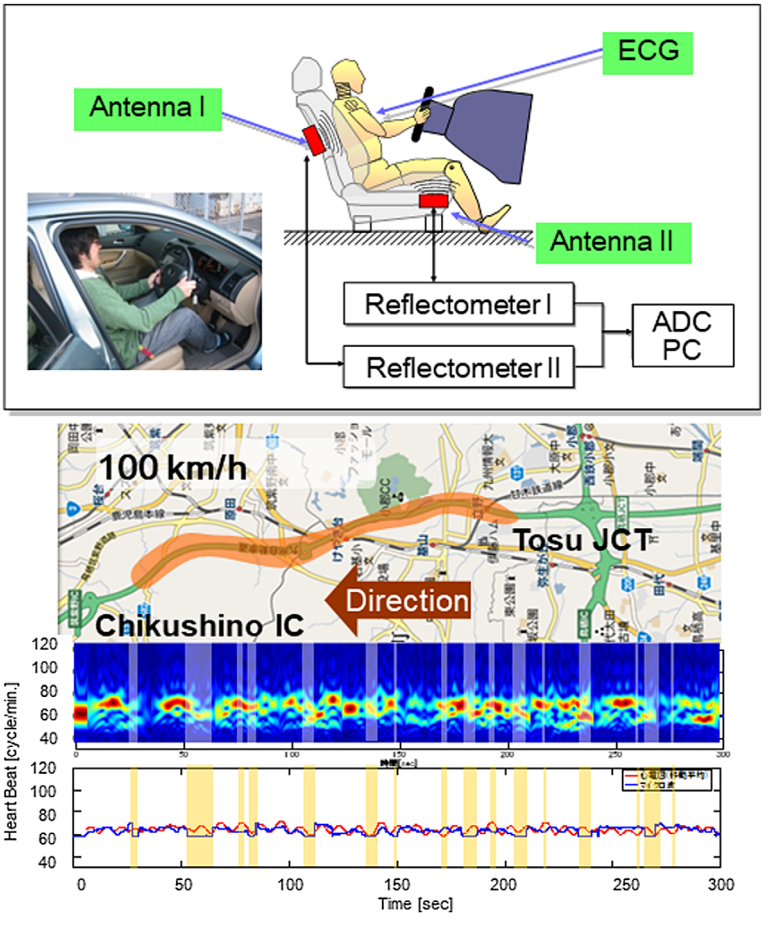

Figure 19. Wavelet spectrum of the reflectometer signal, and comparison of peak value with ECG during driving.

4.1.5. Measurement using 24 GHz module

As for radar modules with frequency of 24 GHz, outdoor use is authorized as a movement body detection sensor when the radiation power is low. Low cost, commercial made 24 GHz modules are being applied to the HR measurement and the HRV evaluation using the above mentioned algorithm. The measurements are performed for a subject working using a PC. Figure 20 shows the comparison of heart rate obtained by a reflectometer and an ECG for both instantaneous value and 30 s averaged value of peak interval (corresponding to R–R interval). Here, a template and cross-correlation algorithm is used to obtain R–R intervals from raw reflectometer signals. It is noted that the instantaneous values are ±15% deviation between with each other; however, the average values are in good agreement (within 1%) with each other. Figures 21 and 22 show the real-time measurements of HR and HRV using the template and cross-correlation algorithm. A template is obtained by accumulating 30 s of data, and the analyzing window is shifted every 2 s. In Figure 21, the mental stress (a flash calculation test) and the physical stress (an ice test) are applied to a subject during the time of 75–115 ms and 40–80 ms, respectively. It is shown that the time evolution of HR obtained by a reflectometry is in good agreement with that by an ECG, also that the values of HR and LF/HF increase and that of CVRR decreases during the stress condition. Generally speaking, the LF component agrees with not only the value but also the time behavior (Figure 22). However, the HF component often does not agree, because the reflectometer signal includes numerous high-frequency fluctuations due to body movement. This is the reason why the absolute values of CVRR and LF/HF disagree, that is, the values of CVRR obtained by a microwave reflectometer is larger than that obtained by an ECG, and LF/HF is smaller in microwave

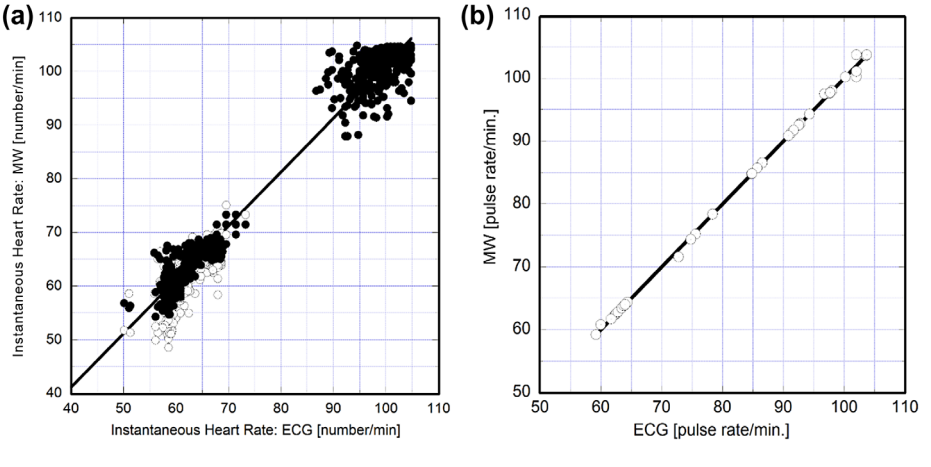

Figure 20. Comparison of heart rate obtained by a 24 GHz microwave sensor and an ECG. A template and cross-correlation algorithm is utilized to obtain the time evolution of R-R intervals. (a) Comparison of instantaneous R-R intervals, and (b) 30 s average of R-R intervals.

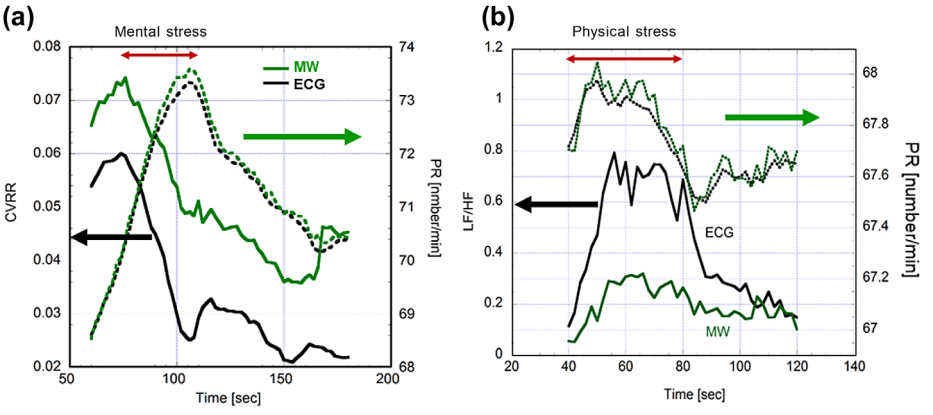

Figure 21. Real-time measurement of HR and HRV during stress application to a subject. A template and cross-correlation algorithm is used to obtain R–R intervals from raw signals obtained by a 24 GHz microwave reflectometer and an ECG. (a) The mental stress (flash calculation test) is applied during 75–115 ms. (b) The physical stress (ice test) is applied during 40–80 ms.

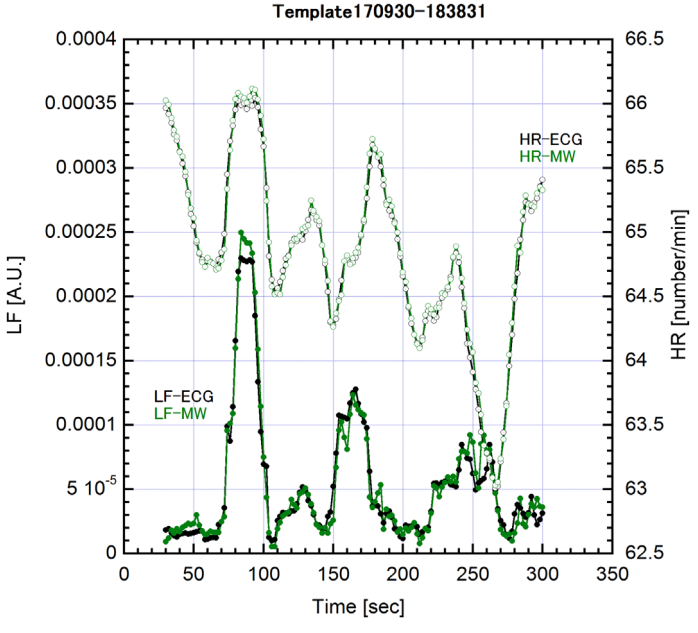

Figure 22. Real-time measurement of HR and HRV by a 24 GHz microwave sensor and an ECG. A template and cross-correlation algorithm is used to obtain R–R intervals from raw signals.

reflectometry. However, the time behavior of CVRR and LF/HF agrees with each other. Therefore, the identification of human's mental and physical state will be still possible.

By combining microwave reflectometry and the HRV evaluation algorithms mentioned above, it is seen that the time behaviors of HR, LF/HF, and CVRR are

obtained, which can be utilized to find the mental and physical conditions of a subject. This potential will become useful for evaluation of an automobile driver's state as support for autonomous operation in near future.

4.2. Microwave imaging reflectometry for breast cancer detection

4.2.1. Motivation

Breast cancer incidence increases each year although mortality remains at the similar level due to the progress in medical treatment and the increase of the inspection rate [84]. It is most important to detect early stage tumors for healing. X-ray mammography is currently used for breast cancer detection. However, there is a limit to detection sensitivity of mammography especially for younger women, since mammography images the density of the breast to find suspicious areas. Also, breast compression required for clear images with mammography often causes pain to patients. Microwave imaging utilizes contrast of dielectric constant between malignant and normal breast tissues.

In microwave region, the contrast of dielectric constant is said to be as large as 10:1 [85], and the attenuation of electromagnetic wave in normal breast tissue is comparatively small. A burden to patients will be reduced by applying a microwave tomography method or an ultra-wideband (UWB) radar to breast imaging since it can perform contactless inspection. Therefore, the breast imaging with microwave imaging has the potential to be used concomitantly with X-ray mammography [86]. For a reference, the electric field distribution in the breast region of a human body (Japanese adult woman) is shown in Figure 23. It is calculated using FDTD (finite difference time domain) code. The human body model is offered by National Institute of Information and Communications Technology, Japan (NICT) [72]. It is obvious that lower frequency microwaves (5, 10 GHz) penetrate into the human body compared to high-frequency microwave (24 GHz). This result is also related to Section 3.1.

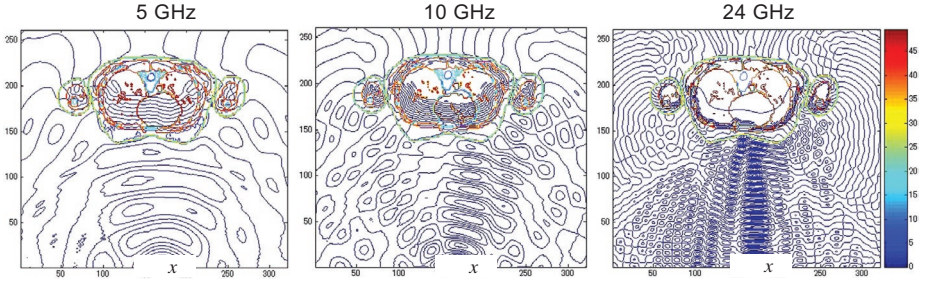

Figure 23. Distribution of electromagnetic waves in a human body obtained by FDTD calculation for various frequencies.

4.2.2. Reconstruction method of imaging and apparatus

The optical properties of a material are generally characterized by the complex permittivity. A foreign object having a permittivity different from an object to be inspected causes wave reflection and scattering. The breast has lower dielectric constant and loss tangent than the other parts of the human body. In addition, the dielectric properties of breast tumors are much higher than the normal breast tissue. We assume that the dielectric property of normal breast tissue is $\varepsilon_r = 9$, $\sigma = 0.4$ S/m and that of the malignant breast tissue is $\varepsilon_r = 50$, $\sigma = 4$ S/m [87,88].

A schematic of a UWB radar is shown in Figure 24. A probe beam is an 8 V, 65 ps FWHM pulse. The FFT spectrum extends to −10 GHz. The impulse is fed to a planar-type antenna. The reflected wave detected by an identical antenna is recorded by a high-speed sampling scope. The antennas attached to a rotational stage with a stepping motor are moved every 5 degrees around the breast model from 0 to 180 degrees through the top. The reflected waves from the breast model are received at each antenna location; thus, 37 reflected waves are provided. For the present experiment, we use a phantom model simulated for an actual breast biopsy (CRIS: model 051). This distance between the antennas and the phantom provides a reasonable coverage of a model by an antenna radiation pattern. Dielectric materials with 6–9 mm diameter used as tumors are located at around 10–25 mm depth from the top of the breast model. The antennas should efficiently focus the microwave signal toward the target and collect the back-scattered power. A wideband antenna with unidirectional radiation pattern is required for these applications. Moreover, the antenna should be sufficiently compact for easy installation, integration with other electronic circuits, and ease in fabrication of the arrays. Microstrip antennas are compact, but they exhibit narrow bandwidth.

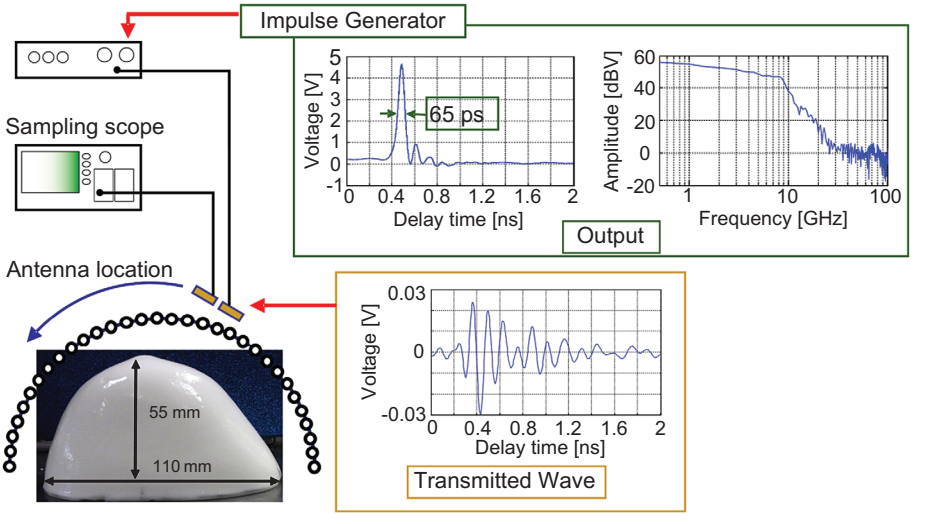

Figure 24. Experimental apparatus of the ultrashort-pulse reflectometer (from Ref. [83]). Copyright 2012 IOP Publishing.

This renders them unsuitable for time domain applications. The Vivaldi antenna is selected because it provides wideband characteristics with acceptable performance as the present frequency response.

4.2.3. Results and status of microwave imaging

Considering the frequency band to affect the image reconstruction, we have selected the results in several frequency bandwidths from 2–7 GHz to 2–10 GHz [88,89]. When we set the frequency bandwidth as 5–8 GHz but shift the start frequency from 2 to 5 GHz, the clutter increases and imaging becomes unclear for the start frequency of higher than 4 GHz [90].

The image reconstruction method called confocal microwave imaging (CMI) is based on a synthetic aperture radar (SAR) [89–92]. Before an image formation, the tumor response must be extracted from the measurement data efficiently. The data contain additional undesired signals such as the antenna coupling, the reflections from the skin, and the tumor response. Usually, we can subtract all the unwanted signals by the measured signal without the tumor. This method is called background subtraction. It can be considered as the ideal way of extracting tumor response. However, this method cannot be used with real patients. The phantom model is covered by a similarly shaped cover made by a material with similar dielectric constant. It is also important to minimize the gap between the cover and the phantom model. Since most of the reflected waves occur from a cover surface, we can subtract the component by measuring the reflected waves only with the cover beforehand.

The reflected waves from the surface of the breast model and the object can be seen in Figure 25(a). The image reconstruction is performed after removing the ringing components from this remaining signal. Figure 25(b) shows an example of the reconstructed image for the frequency band of 1–10 GHz where the permittivity of the targets is at 20.

The breast cancer will be detected by the UWB radar when the tumor is separated from the irregular mammary gland or the mammary gland is not very dense. Otherwise, the detection becomes even more difficult, and the reconstruction of the cancer shape will be impossible. The microwave tomography will be the candidate to resolve this problem [93–98].

5. Application to remote sensing

5.1. Synthetic aperture radar (SAR) using microwave

In Section 2 the spatial resolution of a real aperture radar is discussed in the azimuth (cross-range) direction as well as in the range direction. The cross-range resolution corresponds to the beam width in the azimuth direction $\Delta x = W_0 = R\lambda/D_A$. This value becomes relatively large, for example, $\Delta x = R\lambda/D_A = 100$ m for $\lambda = 2$ cm, $R = 1000$ m, and $D_A = 20$ cm. In order to obtain the resolution of $\Delta x = 1$ m, the required antenna size becomes 20 m, which is rather impractical.

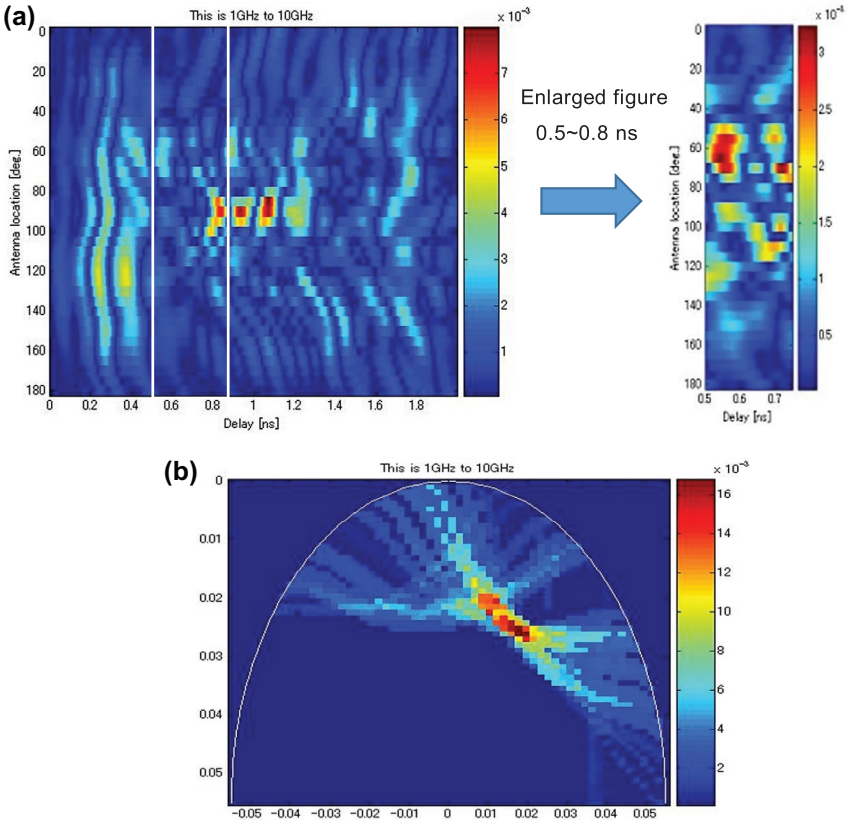

Figure 25. Image reconstruction: (a) reflected waves at each position, (b) reconstruction of the object. The object's permittivity is $\varepsilon_r = 20$ (from Ref. [83]). Copyright 2012 IOP Publishing.

One of the methods to solve this problem is to use the idea of synthetic aperture radar (SAR) [99–103]. In a conventional SAR called stripmap-mode SAR, the position of the antenna remains fixed relative to a platform such as an aircraft, illuminating a strip of terrain as it flies. The processing of the returned signals allows the effective synthesis of a very large antenna. Since the effective antenna size $D_s \cong R\Delta\theta = 2R\lambda/D_A$ ($\Delta\theta = 2\lambda/D_A$ is the radiation angle of an antenna), the cross-range resolution becomes $\Delta x \cong D_A/2$. Therefore, the resolution is given by the half aperture size of a radiation antenna, and does not depend on the distance from an antenna to an object. Airborne and satellite-based SARs are capable of producing images of the land targets and the ground terrain in all weather conditions and during the night. Thus, the SAR produces complex images that enable us to view sub-wavelength changes of the targets.

There exists another type SAR called spotlight-mode SAR which utilizes a tomographic reconstruction technique. The microwave illuminates a target area from different perspectives. When the longitude and the latitude of the reference point are provided, 'three-dimensional earth location information of the point'

can be decided from the database. The distance between the platform and the reference point is decided by the GPS (global position system) [104,105]. The spotlight mode SAR takes radar data in a way that the Fourier transform of raw data forms complex images. It has an advantage that the radar will be usable on unmanned-airplane and helicopters.

In the next section, a spotlight-mode SAR fabricated as universities project named 'Live SAR' [105] is introduced. Live SAR takes image data in wide squint angle ranges from −45 to 45 degrees instead of only broad-side (squint angle of ±90), and enables us to obtain high image resolution of 0.1 m. The images are formed in a few seconds after completion of synthetic aperture data taking, which practically makes real time monitoring practical.

5.1.1. Schematic of the Live SAR

Live SAR is a frequency-chirped radar equipped with a position sensor (combination of GPS and inertia measurement unit (IMU)). It takes images around the motion compensation point (MCP). Total mass of Live SAR system is 25 kg, which is enough light for boarding on light planes and helicopters. Interferometric measurements are performed with the aid of the phase compensation corresponding to MCP-antenna phase center distances. Live SAR consists of electronics assembly and an antenna system on a gimbal as shown in Figure 26. Operation parameters are: chirp width = 1.6 GHz at Ku-band (K-under band, the frequency of 12–18 GHz), microwave power = 7 W, antenna gain = 27 dB, and nominal range <15 km. Based on the position measurements, the antenna points MCP during the radar motion.

Live SAR is controlled by the user-interface software on a laptop (mobile) PC as well as by ground-based computers through Ethernet data link. Users can set

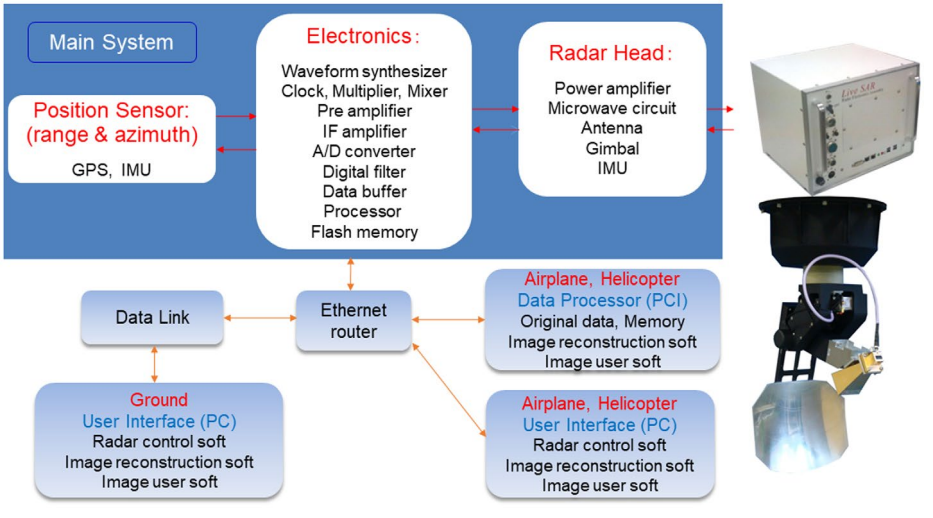

Figure 26. Schematic of the Live SAR system.

the resolution and MCP by clicking any spot within two fan-shaped areas, which are displayed on the map. Software forms complex SAR images soon after raw IQ data are received by the PC. In addition to the images of static targets, images of moving targets and range speeds are obtained. The SAR data exploitation software is run on any linked computers.

5.1.2. Test experiment of the system

The test of Live SAR is performed on a helicopter. Figure 27 (right) shows an example of image near the Kinugawa River taken from a helicopter. The dark areas correspond to the river or the pond water. Figure 27 (left) shows the optical Google Earth image of the area where the SAR image is taken. Since both images are taken in different seasons, different shapes of water areas are observed.

The best expected resolution is around 10–30 cm. Since the frequency and the bandwidth are assigned by the Administration of Radio under the Ministry of Internal Affairs and Communications, the bandwidth is limited to within 1.6 GHz. Therefore, it is difficult to obtain a spatial resolution better than 10 cm. In order to attain the resolution in the range of 1–10 cm, much wider bandwidth will be needed.

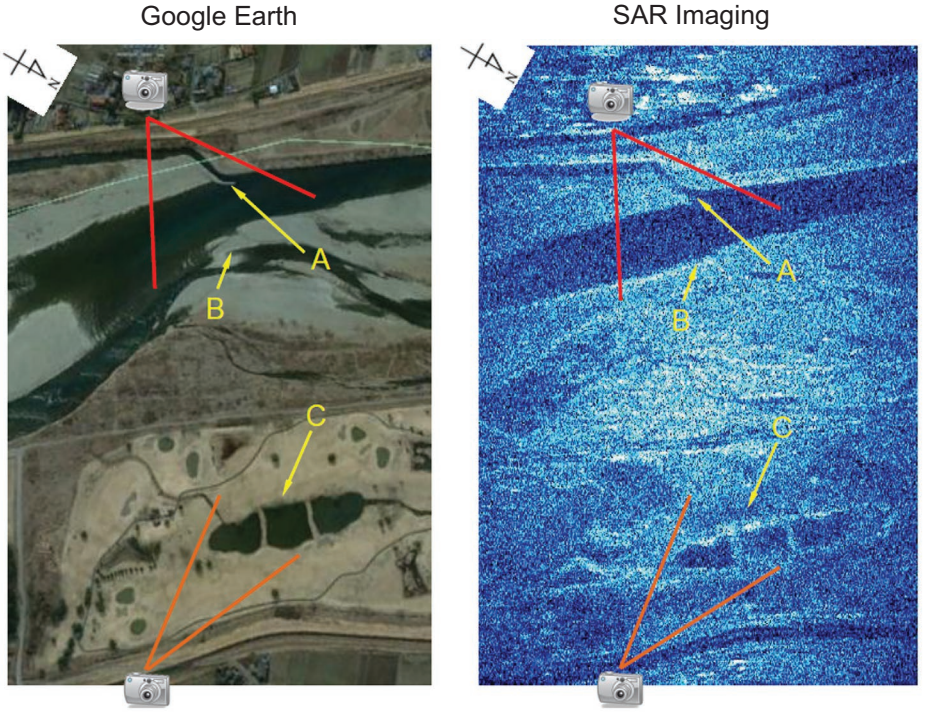

Figure 27. SAR Operation using helicopter. (from Ref. [105]). Copyright 2013 The Institute of Electronics, Information and Communication Engineering.

5.2. Microwave-modulated laser radar

5.2.1. Motivation

An ultra-wideband microwave-modulated laser radar is designed and fabricated for improvement of spatial resolution both in the range direction and in the azimuth direction. The amplitude modulation in a range of 0.01–18 GHz is applied to an infrared laser source of 1550 nm wavelength, which is much wider than previous microwave SAR since there is no bandwidth limitation in the infrared region.

There are several benefits in the imaging diagnostics using microwave-modulated laser. For example, speckle is one of the serious problems for obtaining good signal to noise ratio in the microwave region. This problem can be eliminated because an IR laser output is used as a carrier wave. The drop of coherence length which becomes a problem in laser radar can also be neglected since the data processing is always performed in modulated microwave region. Compared to the radiation pattern of microwave antennas, there is no side lobe in laser beam transmission which degrades the quality of SAR image.

Recently, several research papers [106–109] have been published on frequency-modulated continuous-wave (FM-CW) lidar (laser radar) system and proof-of -principle experiment of imaging formation. The following section introduces an example of this technology. In this section, one of the present ideas is applied to obtain 3D imaging in good spatial resolution as less than 1 cm.

5.2.2. System description of laser radar

Figure 28 shows a schematic diagram of microwave-modulated laser radar. An infrared wave (1550 nm, 5–7 mW) is modulated by an output of a vector network analyzer (VNA). The modulated wave is amplified by a fiber amplifier and irradiated by a transmitting optics (one inch diameter fiber collimator). The reflected wave from an object is picked up by a receiving optics and fed to the VNA via two fiber amplifiers and a band-pass filter with 1 nm bandwidth for improvement of signal to noise ratio. All of the optical fibers are the type of single mode fiber having

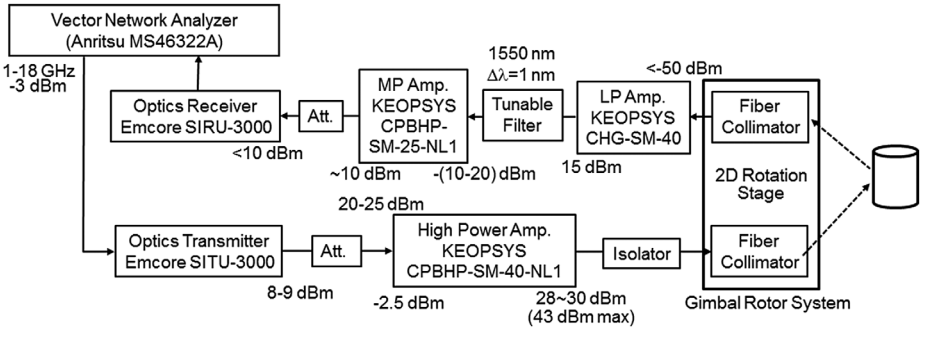

Figure 28. Schematic of the microwave-modulated laser radar (from Ref. [109]). Copyright 2016 International Society for Optical Engineering.

a core diameter of 9–10 μm. The S_{21} component of the VNA is utilized to obtain 3D images of an object. The transmitting and the receiving optics are installed either in a 2D rotation stage or a gimbal rotor stage. In the present experiment, a 2D rotation stage is utilized for 3D imaging formation. A spot-light mode SAR similar to the previous Ku-band system is being fabricated using a gimbal rotor stage with an IMU sensor.

Since the amplitude of the infrared wave is modulated by microwave, the laser output E_0 is given by,

$$\begin{aligned} E_O &\propto \left\{1 + K\sin\left(\omega_m t + \varphi\right)\right\}\cos\left(\omega_0 t + \phi\right) \\ &= \cos\left(\omega_0 t + \phi\right) + K\sin\left(\omega_m t + \varphi\right)\cos\left(\omega_0 t + \phi\right) \end{aligned} \tag{22}$$

where K is the modulation degree, ω_{m} is the total modulation frequency, and φ is the phase difference of microwave. The reflected wave is square-law detected using a wideband photo diode in an optics receiver. Therefore, the modulated microwave component in the reflected wave is given by,

$$P_r \propto K\sin\left(\omega_m t + \varphi\right) \tag{23}$$

and

$$\varphi = kz + \varphi_0 = \left(\omega_m / c\right)z + \varphi_0\,, \quad \omega_m = (\Delta\omega/\Delta t)\tau \tag{24}$$

where c is the speed of light, $\Delta\omega/\Delta t$ is the frequency modulation rate, and z is the distance between a reference position and an object. Using the reference position L_r as an initial value, eq. (24) becomes

$$\varphi = \frac{(\Delta\omega/\Delta t)\tau}{c}\left(z - L_r\right) + \varphi_0 \tag{25}$$

The distance z is obtained by the phase of S_{21}. Since the (x, y) coordinate is given by the laser irradiation center, a 3D imaging of an object is obtained by analyzing the phase component.

A bistatic (separated transmission and receiver optics) arrangement is utilized in the present experiment. The most difficult point for the bistatic system is an optical alignment and its reproducibility, since the reflected wave detected by a lens has to be focused onto a single-mode fiber attached to a fiber collimator. If the position of an object is moved, that is, the distance from a transmitter to a receiver is changed, the alignment of the reflected wave path is shifted. Careful alignment is needed every time the distance is changed. As an improvement, a bistatic system with a beam splitter is utilized in order to minimize the shift of the optical axis [109].

5.2.3 Imaging of the object

In the course of the time interval (τ), the phase of the reflected wave (S_{21} of VNA) varies as given by Equation (24). When the position of the object is changed, it also varies linearly. In order to check the resolution in the range direction, the VNA is operated in the time domain mode (TDR measurement). The measured spatial resolution 0.8 cm is in good agreement to the value of $c/2\,f_m$ which is given in the TDR measurement, where $f_m = \omega_m/2\pi = 18$ GHz is the modulation frequency.

A two-dimensional rotation stage is used to obtain 3D imaging of the object. Conventional frequency domain measurement gives a linear phase change of S_{21} at a fixed reflection point (z). The phase shift in the fixed time interval or the gradient $\Delta f/\Delta t$ changes depending on the value of z. The position (x, y) can be determined by controlling the rotation stage. Thus, we can evaluate the point (x, y, z) on the three-dimensional coordinate. Figure 29 shows examples of the imaging. The spatial resolution in the (x, y) coordinate (azimuth direction) depends on the minimum accuracy of the rotation stage ($10[\mathrm{m}] \times \tan(0.02) = 3.5[\mathrm{mm}]$). The resolution in the z-direction depends on the phase resolution of present software program, which is shown in the bottom figure as contour (~2 mm).

The present system is being applied to a spotlight-mode SAR. In Ref. [108], synthetic aperture imaging has been performed using an FM-CW ladar (the so-called

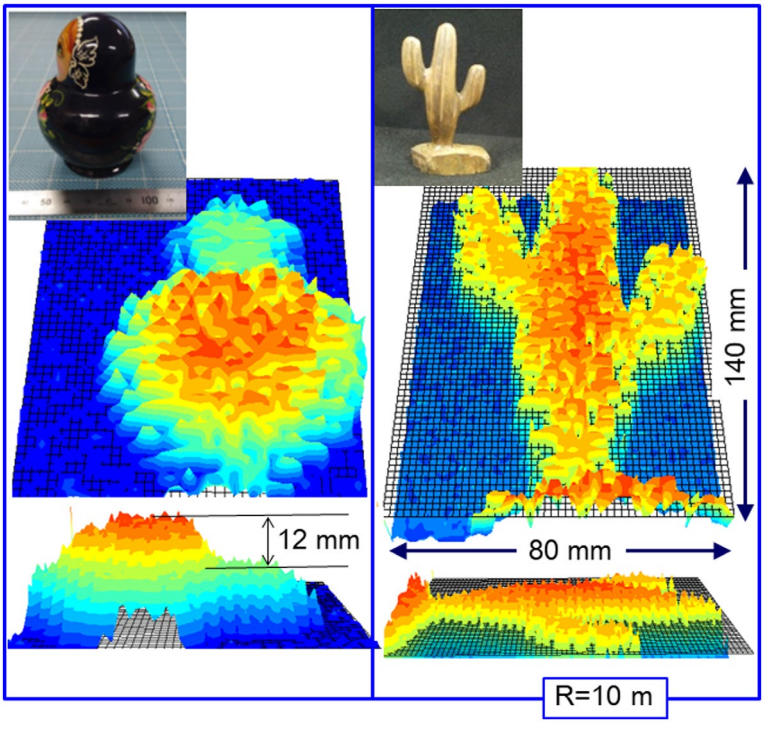

Figure 29. Examples of 3D imaging of objects.

lidar). Bandwidth and output power of an IR laser (1.55 μm) are 3.8 GHz and ~10 W, respectively. The spatial resolution of 4 cm is obtained at the distance of 1 km. By a combination of a microwave SAR and a laser SAR, the range of distance, 0.1–10 km can be covered as a remote imaging system. This will be quite suitable for a wide range of usage such as for observation of disaster points and for disaster prevention.

6. Conclusions

The rapid development of microwave and millimeter-wave technologies has made possible advanced diagnostics for application to various fields. Specifically, active radar reflectometry has become important in various applications due to the possibility of high localization and accessibility of the measurements as well as the non-invasive nature of the systems. In this paper, recent developments and applications of radar reflectometers are described. The key words are profile reflectometry, fluctuation reflectometry, imaging radar (optics imaging and synthetic aperture imaging), and radio-optics fusion technology in order to improve the spatial resolution.

It is seen that various physics issues become clear using radar reflectometry. The lack of spatial resolution due to long wavelength in comparison with visible light has been improved using ultra-wideband modulation (FM & AM) and synthetic aperture processing. The spatial resolution could also be improved in near future by use of metamaterial technologies (metalens, etc.). The radar (reflectometry) diagnostics using microwave/millimeter-wave to infrared wave will have the potential to play the role of crosslink between physics and engineering, and between medicine and engineering because of the advantages of transmissivity, good spatial and temporal resolution, and non-invasive nature due to low energy.

Disclosure statement

No potential conflict of interest was reported by the authors.

Funding

This work was supported by the Grant-in Aid for Scientific Research, The Ministry of Education, Science, Sports, and Culture, Japan [grant numbers 20360186, 26289126, and 17K01310]; the Strategic Information and Communications R&D Promotion Program (SCOPE), The Ministry of Internal Affairs and Communications, Japan [grant numbers 121810001]; Adaptable and Seamless Technology Transfer Program through Target-Driven R&D, Japan Science and Technology Agency [grant number AS2311355F]; and US DoE [grant numbers DE-AC02-09CH11466, DE-FG02-99ER54531, and DE-SC0012551. It is also performed with the support and under the auspices of the NIFS Collaboration Research program [grant numbers NIFS10KCHH029, NIFS16KLEP019].

References

[1] M. Skolnik, *Radar handbook*, McGraw Hill, New York, NY, 1970.
[2] K.W. Kim, E.J. Doyle, W.A. Peebles, A. Ejiri, N.C. Luhmann Jr and C.L. Rettig, Rev. Sci. Instrum. 66 (1995) p.1229.
[3] T. Tokuzawa, A. Mase and N. Oyama, Rev. Sci. Instrum. 70 (1999) p.1068.
[4] J. Santos, M. Manso, P. Varela, J. Neuhauser and the ASDEX group, Rev. Sci. Instrum. 74 (2003) p.1489.
[5] C. Laviron, A.J.H. Donné, M.E. Manso and J. Sanchez, Plasma Phys. Control. Fusion 38 (1996) p.905.
[6] R.B. Morales, S. Hacquin, S. Heuraux and R. Sabot, Rev. Sci. Instrum. 88 (2017) p.043503.
[7] S. Kubota, R. Majeski, W.A. Peebles, R.E. Bell, D.P. Boyle, R. Kaita, T. Kozub, M. Luchia, E. Merino, X.V. Nguyen, T.L. Rhodes and J.C. Schmitt, Rev. Sci. Instrum. 88 (2017) p.053502.
[8] J. Sanchez, B. Branas, T. Estrada, E. de la Luna and V. Zhuravlev, Rev. Sci. Instrum. 63 (1992) p.4654.
[9] A.J.H. Donné, S.H. Heijnen and C.A.J. Hugenholtz, Fusion Eng. Des. 34–35 (1997) p.73.
[10] C.W. Domier, N.C. Luhmann Jr, A. Chou, W.M. Zhang and A.J. Romanowsky, Rev. Sci. Instrum. 66 (1995) p.399.
[11] L.G. Bruskin, A. Mase, T. Tokuzawa, N. Oyama, A. Itakura and T. Tamano, Jpn. J. Appl. Phys. 36 (1997) p.L632.
[12] M. Nagatsu, A. Fuse and A. Mase, Plasma Phys. Control. Fusion 38 (1996) p.1033.
[13] P. Varela, M.E. Manso, A. Silva, the CFN Team, and the ASDEX Upgrade Team, Nucl. Fusion 46 (2006) p.S693.
[14] C.L. Rino, Radio Sci. 14 (1979) p.1135.
[15] A. Silva, M. Manso, P. Varela, L. Cupid and L. Meneses, Rev. Sci. Instrum. 77 (2006) p.10E932.
[16] G.D. Conway, Nucl. Fusion 46 (2006) p.S665.
[17] F. Clairet, S. Heuraux, C. Bottereau, D. Molina, L. Ducobu, F. Leroux and A. Barbuti, Rev. Sci. Instrum. 81 (2010) p.100903.
[18] E. Blanco and T. Estrada, Plasma Phys. Control. Fusion 55 (2013) p.125006.
[19] P.B. Quental, H. Policarpo, R. Luis and P. Varela, Rev. Sci. Instrum. 87 (2016) p.11E720.
[20] T.L. Rhodes, K. Barada, W.A. Peebles and A. Crocker, Rev. Sci. Instrum. 87 (2016) p.11E726.
[21] T. Windisch, A. Krämer-Flecken, J.L. Velasco, A. Könies, C. Nührenberg, O. Grulke, T. Klinger and the W7-X team, Plasma Phys. Control. Fusion 59 (2017) p.105002.
[22] E. Gusakov, M. Irzak and A. Popov, Plasma Phys. Control. Fusion 56 (2014) p.025009.
[23] J.R. Pinzón, T. Happel, E. Blanco, G.D. Conway, T. Estrada and U. Stroth, Plasma Phys. Control. Fusion 59 (2017) p.035005.
[24] C. Lechte, G.D. Conway, T. Görler, C. Tröster-Schmid and the ASDEX Upgrade Team, Plasma Phys. Control. Fusion 59 (2017) p.075006.
[25] G. Hornung, F. Clairet, G.L. Falchetto, R. Sabot, H. Arnichand and L. Vermare, Plasma Phys. Control. Fusion 55 (2013) p.125013.
[26] T. Tokuzawa, S. Inagaki, A. Ejiri, R. Soga, I. Yamada, S. Kubo, M. Yoshinuma, K. Ida, C. Suzuki, K. Tanaka, T. Akiyama, N. Kasuya, K. Itoh, K. Watanabe, H. Yamada, K. Kawahata and LHD Experiment Group, Plasma Fusion Res. 9 (2014) p.1402149.
[27] E.J. Doyle, R.J. Groebner, K.H. Burrell, P. Gohil, T. Lehecka, N.C. Luhmann Jr, H. Matsumoto, T.H. Osborne, W.A. Peebles and R. Philipona, Phys. Fluids B 3 (1991) p.2300.
[28] T. Tokuzawa, Nucl. Fusion 57 (2017) p.025001.

[29] A.B. Altukhov, A.D. Gurchenko, E.Z. Gusakov, L.A. Esipov, M.A. Irzak, M. Yu Stepanov, D.V. Kouprienko, S.I. Lashkul, S. Leerink, P. Niskala, A. Yu Stepanov and N.V. Teplova, Plasma Phys. Control. Fusion 58 (2016) p.105004.
[30] T. Windisch, A. Krämer-Flecken, J.L. Velasco, A. Könies, C. Nührenberg, O. Grulke, T. Klinger and the W7-X team, Plasma Phys. Control. Fusion 59 (2017) p.105002.
[31] E. Mazzucato, Nucl. Fusion 41 (2001) p.203.
[32] E. Mazzucato, T. Munsat, H. Park, B.H. Deng, C.W. Domier, N.C. Luhmann Jr, A.J.H. Donné and M.J. van de Pol, Phys. Plasmas 9 (2002) p.1955.
[33] H. Park, C.C. Chang, B.H. Deng, C.W. Domier, A.J.H. Donné, K. Kawahata, C. Liang, X.P. Liang, H.H. Lu, N.C. Luhmann Jr, A. Mase, H. Matsuura, E. Mazucatto, A. Miura, K. Mizuno, T. Munsat, Y. Nagayama, M.J. van de Pol, J. Wang, Z.G. Xia and W.-K. Zhang, Rev. Sci. Instrum. 74 (2003) p.4239.
[34] G.J. Kramer, R. Nazikian and E.J. Valeo, Plasma Phys. Control. Fusion 46 (2004) p.695.
[35] K.J. Brunner, J.C. Chorley, N.A. Dipper, G. Naylor, R.M. Sharples, G. Taylor, D.A. Thomas and R.G.L. Vann, Rev. Sci. Instrum. 87 (2016) p.11E129.
[36] T. Munsat, E. Mazzucato, H. Park, B.H. Deng, C.W. Domier, N.C. Luhmann Jr, J. Wang, Z.G. Xia, A.J.H. Donné and M.J. van de Pol, Rev. Sci. Instrum. 74 (2003) p.1426.
[37] M. Ignatenko, A. Mase, L.G. Bruskin, Y. Kogi and H. Hojo, Nucl. Fusion 46 (2006) p.S760.
[38] H. Hojo, Y. Kurosawa and A. Mase, Rev. Sci. Instrum. 70 (1999) p.983.
[39] T. Yoshinaga, Y. Nagayama, D. Kuwahara, H. Tsuchiya, S. Yamaguchi, Y. Kogi, S. Tuji-Iio, H. Hojo and A. Mase, Plasma Fusion Res. 5 (2010) p.030.
[40] B. Tobias, G.J. Kramer, E. Valeo, C.M. Muscatello, X. Ren, M. Chen, A.G. Spear, A.V. Pham, T. Phan, M. Mamidanna, J. Lai, M. Li, D. Fu, C.W. Domier, N.C. Luhmann Jr, X. Chen, N. Ferraro, A. Garofalo, S. Zemedkun, T.L. Munsat and Y. Zhu, Proc. Sci., 1st EPS Conf. on Plasma Diagnostics, Frascati (2015).
[41] B.J. Tobias, M.E. Austin, J.E. Boom, K.H. Burrell, I.G.J. Classen, C.W. Domier, N.C. Luhmann Jr, R. Nazikian and P.B. Snider, Rev. Sci. Instrum. 83 (2012) p.10E329.
[42] C.M. Muscatello, C.W. Domier, X. Hu, G.J. Kramer, N.C. Luhmann Jr, X. Ren, P. Riemenschneider, A. Spear, B.J. Tobias, E. Valeo and L. Yu, Rev. Sci. Instrum. 85 (2014) p.11D702.
[43] D. Kuwahara, N. Ito, Y. Nagayama, T. Yoshinaga, S. Yamaguchi, M. Yoshikawa, J. Kohagura, S. Sugito, Y. Kogi and A. Mase, Rev. Sci. Instrum. 85 (2014) p.11D805.
[44] N. Ito, D. Kuwahara, Y. Nagayama, M. Yoshikawa, J. Kohagura, S. Sugito, A. Mase, Y. Kogi, T. Yoshinaga and S. Yamaguchi, Plasma Fusion Res. 10 (2015) p.3402034.
[45] D. Kuwahara, N. Ito, Y. Nagayama, H. Tsuchiya, M. Yoshikawa, J. Kohagura, T. Yoshinaga, S. Yamaguchi, Y. Kogi and A. Mase, J. Instrum. 10 (2015) p.C12031.
[46] Y. Nagayama, S. Yamaguchi, Z. Shi, H. Tsuchiya, S. Hashimoto, N. Ito, M. Jiang, D. Kuwahara and S. Sugito, Plasma Fusion Res. 11 (2016) p.2402111.
[47] Y. Nagayama, N. Ito, D. Kuwahara, H. Tsuchiya and S. Yamaguchi, Rev. Sci. Instrum. 88 (2017) p.044703.
[48] X. Ren, M. Chen, X. Chen, C.W. Domier, N.M. Ferraro, G.J. Kramer, N.C. Luhmann Jr, C. M. Muscatello, R. Nazikian, L. Shi, B.J. Tobias and E. Valeo, J. Instrum. 10 (2015) p.P100036.
[49] Y. Wang, B. Tobias, Y.T. Chang, J.H. Yu, M. Li, F. Hu, M. Chen, T. Phan, A.V. Pham, Y. Zhu, C.W. Domier, L. Shi, E. Valeo, G.J. Kramer, D. Kuwahara, Y. Nagayama, A. Mase and N.C. Luhmann Jr, Nucl. Fusion 57 (2017) p.072007.
[50] W. Lee, J. Leem, G.S. Yun, H.K. Park, S.H. Ho, W.X. Wang, R.V. Budny, N.C. Luhmann Jr and K.W. Kim, Rev. Sci. Instrum. 87 (2016) p.11E134.

[51] Y.L. Zhu, J.L. Xie, C.X. Yu, Z.L. Zhao, B.X. Gao, D.X. Chen, W.D. Liu, W. Liao, C.M. Qu, C. Luo, X. Hu, A.G. Spear, N.C. Luhmann Jr, C.W. Domier, M. Chen, X. Ren and B.J. Tobias, Rev. Sci. Instrum. 87 (2016) p.11D901.
[52] J.M. Mazurek and G. Syamlal, MMWR Morb Mortal Wkly Rep. 67 (2018) p.377. It is described that 8.2% of U.S. adults have current asthma.
[53] M.J. Gurka, S.L. Filipp and M.D. DeBoer, Nutr. Diabetes 8 (2018) p.14. The diabetes and diabetes wannabees are said to be approximately 30% of adults.
[54] B.A. Williams, A.M. Honushefsky and P.B. Berger, Am. J. Cardiol. 120 (2017) p.1961. It is described that the prevalence is 4-6% limiting to arrhythmia (atrial fibrillation).
[55] J.C. Lin, Proc. IEEE 63 (1975) p.1530.
[56] P.C. Pedersen, C.C. Johnson, C.H. Durney and D.G. Bragg, IEEE Trans. Biomed. Eng. 23 (1976) p.410.
[57] D.W. Griffin, Microwave J. 21 (1978) p.69.
[58] J.C. Lin, J. Kiernicki, M. Kiernicki and P.B. Wollschlaeger, IEEE Trans. Microw. Theory Tech. 27 (1979) p.618.
[59] K.-M. Chen, D. Misra, H. Wang, H.-R. Chuang and E. Postow, IEEE Trans. Biomed. Eng. 33 (1986) p.697.
[60] K.-M. Chen, Y. Huang, J. Zhang and A. Norman, IEEE Trans. Biomed. Eng. 27 (2000) p.105.
[61] M. Malik, Circulation 93 (1996) p.1043.
[62] L. Duvnjaek, S. Vuckovic, N. Car and Z. Metelko, J. Diabetes Complications 15 (2001) p.314.
[63] U. Wiklund, M. Akay and U. Niklasson, IEEE Eng. Med. Biol. Mag. 16 (1997) p.113.
[64] E. Landenberger-Leo, Med. Pr. 37 (1986) p.347.
[65] M.F. Hilton, R.A. Bates, K.R. Godfrey, M.J. Chappell and R.M. Cayton, Med. Biol. Eng. Comput. 37 (1999) p.760.
[66] K.C. Bilchick, B. Fetics, R. Djoukeng, S.G. Fisher, R.D. Fletcher, S.N. Singh, E. Nevo and R.D. Berger, Am. J. Cardio. 90 (2002) p.24.
[67] M. Takada, H. Takada and A. Katayama, Hep 32 (2005) p.504.
[68] M. Takada, T. Ebara and Y. Sakaki, HEP. 35 (2008) p.373.
[69] S. Suzuki, T. Matsui, H. Imuta, M. Uenoyama, H. Yura, M. Ishihara and M. Kawakami, Med. Biol. Eng. Comput. 46 (2008) p.709.
[70] T. Maruyama, S. Yasuda and A. Mase, Japan. J. Electrocardiology 35 (2015) p.133(in Japanese) .
[71] N. Tateishi, A. Mase, L. Bruskin, Y. Kogi, N. Ito, T. Shirakata and S. Yoshida, Proc. Asia Pacific Microwave Conf., Bangkok (2007) p.2151.
[72] T. Nagaoka, S. Watanabe, K. Sakura, E. Kunieda, S. Watanabe, M. Taki and Y. Yamanaka, Phys. Med. Biol. 49 (2004) p.1.
[73] D. Nagae and A. Mase, Rev. Sci. Instrum. 81 (2010) p.094301; Virtual J. Biolog. Phys. Res. 20 (2010).
[74] A. Mase and D. Nagae, US Pt. 9186079 (2015).
[75] A.D. Droitcour, O.B. Lubecke, J. Lin and G.T.A. Kvacs, IEEE Trans. Microw. Theory Tech. 52 (2004) p.838.
[76] A.D. Droitcour, PhD. Dissertation, Stanford University (2006).
[77] J.P. Burg, Paper presented at the 37th Ann. Int. Meeting, Soc. of Explor. Geophys., Oklahoma (October 1967) p.9.
[78] See http://cmm.cit.nih.gov/maxent/letsgo.html for the MEM of data analysis.
[79] H. Akaike, Ann. Inst. Statist. Math. 21 (1969) p.243; H. Akaike, Ann. Inst. Statist. Math. 21 (1969) p.407.

[80] P. Burbaud, P. Degreze, P. Lafon, J.M. Franconi, B. Bouligand, B. Bioulac, J.M. Caille and M. Allard, J. Neurophysiol. 74 (1995) p.2194.
[81] H. Mizuhara, L.-Q. Wang, K. Kobayashi and Y. Yamaguchi, NeuroReport 15 (2004) p.1233.
[82] Y. Yoshida, K. Yokoyama and N. Ishii, IEEJ Trans. EIS. 126 (2006) p.1441.
[83] A. Mase, N. Ito, M. Oda, Y. Komada, D. Nagae, D. Zhang, Y. Kogi, S. Tobimatsu, T. Maruyama, H. Shimazu, E. Sakata, F. Sakai, D. Kuwahara, T. Yshinaga, T. Tokuzawa, Y. Nagayama, K. Kawahata, S. Yamaguchi, S. Tsuji-Iio, C.W. Domier, N.C. Luhmann Jr, H.K. Park, G. Yun, W. Lee, S. Padhi and K.W. Kim, J. Instrum. 7 (2012) p.C01089.
[84] M. Ghoncheh, Z. Pournamdar and H. Salehiniya, Asian Pac. J. Cancer Prev. 17 (2016) p.46.
[85] E.J. Bond, X. Li, S.C. Hagness and B.D. Van Veen, IEEE Trans. Antennas Propag. 51 (2003) p.1690.
[86] M. Lazebnik, D. Popovic, L. McCartney, C.B. Watkins, M.J. Lindstrom, J. Harter, S. Sewall, T. Ogilvie, A. Magliocco, T.M. Breslin, W. Temple, D. Mew, J.H. Booske, M. Okoniewski and S.C. Hagness, Phys. Med. Biol. 52 (2007) p.6093.
[87] J. Moll, T.N. Kelly, D. Byrne, M. Sarafianou, V. Krozer and I.J. Craddock, Int. J. Biomed. Imaging 20 (2014) p.943549.
[88] S.C. Hagness, A. Taflove and J.E. Bridges, IEEE Trans. Biomed. Eng. 45 (1998) p.1470.
[89] X. Li and S.C. Hagness, IEEE Microw. Wirel. Co. 11 (2001) p.130.
[90] E.C. Fear, X. Li and S.C. Hagness, IEEE Trans. Biomed. Eng. 49 (2002) p.812.
[91] M. Klemm, I.J. Craddock, J.A. Leendertz, A. Preece and R. Benjamin, IEEE Trans. Antennas Propag. 57 (2009) p.1692.
[92] D. Zhang and A. Mase, Biomed. Eng. Appl. Basis & Commun. 26 (2014) p.1450004.
[93] A. Francois and C. Pichot, IEEE Trans. Antennas Propag. 45 (1997) p.203.
[94] M. Bertero, M. Miyakawa, P. Boccacci, F. Conte, K. Orikawa and M. Furutani, IEEE Trans. Biomed. Eng. 47 (2000) p.690.
[95] T. Takenaka, H. Zhou and T. Tanaka, J. Opt. Soc. Am. 20 (2003) p.1867.
[96] J.E. Johnson, T. Takenaka and T. Tanaka, IEEE Trans. Biomed. Eng. 55 (2008) p.1941.
[97] L. Mohamed, Y. Ono, T. Kamiya, N. Ozawa, and Y. Kuwahara, IEICE Trans. J99-C (2016) p.393 (in Japanese).
[98] Y. Kuwahara, Proc. 11th European Conf. Antennas Propag. (EUCAP) (March 2017) p.1061.
[99] W.M. Brown and L.J. Porcello, IEEE Spectrum 6 (1969) p.52.
[100] J.C. Curlander and R.N. McDonough, *Synthetic Aperture Radar System and Signal Processing*, Wiley, 1991.
[101] D.C. Munson Jr, J.D. O'Brien and W.K. Jenkins, Proc. IEEE. 71 (1983) p.917.
[102] C.V. Jakowatz Jr, D.E. Wahl, P.H. Eichel, D.C. Ghiglia and P.A. Thompson, *Spotlight-Mode Synthetic Aperture Radar: A Signal Processing Approarch*, Springer, 1996.
[103] H. Ikezi, M. Inutake and A. Mase, Eng. Sci. Rep. Kyushu University 29 (2007) p.269.
[104] D.C. Munson Jr, J.D. O'Brien and W.K. Jenkins, Proc. IEEE 71 (1983) p.917.
[105] Y. Kogi, H. Ikezi, A. Mase, N. Ito, M. Sato, A. Suzuki, F. Sakai, S. Mizukami, K. Kamewari and M. Inutake, Proc. 4th Asia-Pacific Conf. on SAR, Tsukuba (September 2013).
[106] S. Gao and R. Hui, Opt. Lett. 37 (2012) p.2022.
[107] X. Wang, A. Mase, H. Ikezi, M. Inutake, Y. Kogi and K. Uchino, J. Eletromag.Waves Appli. 28 (2014) p.917904.
[108] G. Li, R. Wang, Z. Song, K. Zhang, Y. Wu and J. Pan, Appl. Optics 56 (2017) p.3257.
[109] A. Mase, Y. Kogi, H. Ikezi, M. Inutake and X. Wang, Proc. 2016 SPIE: Optical Engineering and Applications 9973 (2016) p.99730G-1.